

CodecNeRF: Toward Fast Encoding and Decoding, Compact, and High-quality Novel-view Synthesis

Gyeongjin Kang^{1*}

Younggeun Lee^{2*}

Seungjun Oh²

Eunbyung Park^{1,2†}

¹Department of Electrical and Computer Engineering, Sungkyunkwan University

²Department of Artificial Intelligence, Sungkyunkwan University

Abstract

Neural Radiance Fields (NeRF) have achieved huge success in effectively capturing and representing 3D objects and scenes. However, several factors have impeded its further proliferation as next-generation 3D media. To establish a ubiquitous presence in everyday media formats, such as images and videos, it is imperative to devise a solution that effectively fulfills three key objectives: fast encoding and decoding time, compact model sizes, and high-quality renderings. Despite significant advancements, a comprehensive algorithm that adequately addresses all objectives has yet to be fully realized. In this work, we present CodecNeRF, a neural codec for NeRF representations, consisting of a novel encoder and decoder architecture that can generate a NeRF representation in a single forward pass. Furthermore, inspired by the recent parameter-efficient finetuning approaches, we develop a novel finetuning method to efficiently adapt the generated NeRF representations to a new test instance, leading to high-quality image renderings and compact code sizes. The proposed CodecNeRF, a newly suggested encoding-decoding-finetuning pipeline for NeRF, achieved unprecedented compression performance of more than 150 \times and 20 \times reduction in encoding time while maintaining (or improving) the image quality on widely used 3D object datasets, such as ShapeNet and Objaverse.

1 Introduction

Neural Radiance Fields (NeRF) have been enormously successful in representing 3D scenes [54]. Given a handful of pictures taken from various viewpoints, it generates photo-realistic images from novel viewpoints, proving beneficial for various applications, such as 3D photography and navigation [34, 27, 33, 1, 36, 51]. In addition, ongoing research endeavors have enhanced its compatibility with conventional graphics rendering engines by enabling mesh and texture extraction [56, 62, 2, 81, 70, 57], and thus, it further expands its usability. Moreover, the recent 3D generation and editing techniques make it more valuable as a next-generation 3D media representation, opening new possibilities and applications.

The primary reason contributing to the longstanding success of image and video is the widespread adoption of standard codec software and hardware [9, 75, 85, 65]. We simply take a picture or video with our hand-held devices, and the encoder rapidly compresses the data. Then, the encoded data are transmitted over network communication channels, and the receivers can consume the data with the help of fast decoding software and hardware. We envision similar usage of 3D media using NeRF: 1) senders obtain multi-view images, 2) an encoder turns those images into a NeRF representation (encoding), 3) the encoded representation is communicated through the network, 4) receivers decode

*Equal contribution.

†Corresponding author.

the encoded data and users enjoy the contents by rendering from various viewpoints. We urge the development of an algorithmic pipeline that can achieve rapid encoding and decoding speeds, compact data sizes, and high-quality view synthesis to support this common practice.

Despite considerable technological progress, there has yet to be a fully satisfying solution to achieve all of the stated goals. Training speed (encoding time) has remarkably advanced from days to a few hours or minutes [14, 21, 31, 55, 78, 76, 22, 45]. However, due to the inherent drawback of the per-scene optimization approach, they still require powerful GPU devices and at least tens of thousands of training iterations to converge. The encoder-decoder approaches, which generate NeRF in a single network forward pass, have been proposed [83, 82, 15, 42, 88, 39, 29, 48, 20, 16, 61, 63]. However, they primarily focus on few-shot generalization and do not consider the codec aspects, and the rendering image quality is limited compared to the optimization-based approaches. On the other hand, there has been extensive investigation into compact NeRF representations to minimize the encoded data sizes [78, 64, 77, 40, 72, 80, 8, 50, 37, 19]. While successful, the suggested methods are mostly based on the per-scene optimization approach, resulting in longer training iterations.

In this work, we introduce CodecNeRF, a neural codec for NeRF designed to accomplish the previously mentioned objectives all at once. The proposed neural codec consists of a novel encoder and decoder architectures that can produce a NeRF representation in a single forward pass. The encoder takes as inputs multi-view images and produces compact codes that are transmitted to other parties through network communications. The decoder that is present on both the sender and receiver sides generates the NeRF representations given the delivered codes. This forward-pass-only approach, as demonstrated numerous times by preceding neural codecs for image and video, can achieve rapid encoding/decoding times and exceptional compression performance.

The forward pass alone, however, does not guarantee that the generated NeRF representation synthesizes high-quality images. The primary issue stems from the scarcity of instances and diversities within the existing 3D datasets, in contrast to the abundance found in image and video domains. This shortage hampers the trained models’ capability to effectively generalize to new 3D test instances. Therefore, we propose to finetune the NeRF representations on the sender side and further transmit the finetuned ‘delta’ information to the receiver along with the codes. Then, the decoder on the receiver side uses the transmitted codes to reproduce the initial NeRF representations and apply ‘delta’ to obtain the final NeRF representations. Since the initial NeRF representations from the forward pass are already well-formed, the subsequent finetuning requires far fewer iterations than the per-scene optimization approach, which results in significantly faster encoding time.

To reduce the overall size of the final code (codes + finetuning ‘delta’), we suggest parameter-efficient finetuning (PEFT) techniques on the initial NeRF representations [24]. Finetuning the entire decoder or NeRF representations substantially increases the code sizes to be transmitted, negating the advantages of employing the encoder and decoder methodology. In this work, the NeRF representation is based on K-planes method consisting of multi-resolution plane features and an MLP network. We employ the widely used low-rank adaptation (LoRA) methods for the MLP and suggest a novel PEFT technique for plane features inspired by the low-rank tensor decomposition method.

We have conducted comprehensive experiments using two representative 3D datasets, ShapeNet [13] and Objaverse [18, 17]. The experimental results show that the proposed encoder-decoder-finetuning method, CodecNeRF, achieved $150\times$ more compression performance and $20\times$ encoding (training) speed up over the per-scene optimization baseline method (triplane) while maintaining the rendered image quality. Additionally, we demonstrate the versatility of CodecNeRF by applying it on real scenes from the DTU dataset [28]. We perceive this outcome as unlocking new research opportunities and application avenues using NeRF. The main contributions can be summarized as follows:

- We propose CodecNeRF, an encoder-decoder-finetuning pipeline for the newly emerging NeRF representation.
- We design novel 3D-aware encoder-decoder architectures, efficiently aggregating multi-view images, generating compact codes, and making NeRF representations from the codes.
- We present the parameter-efficient finetuning approach for further finetuning the NeRF representations that consist of MLP and feature planes.
- We achieved the unprecedented compression ratio and encoding speedup of NeRF while preserving high-quality rendering.

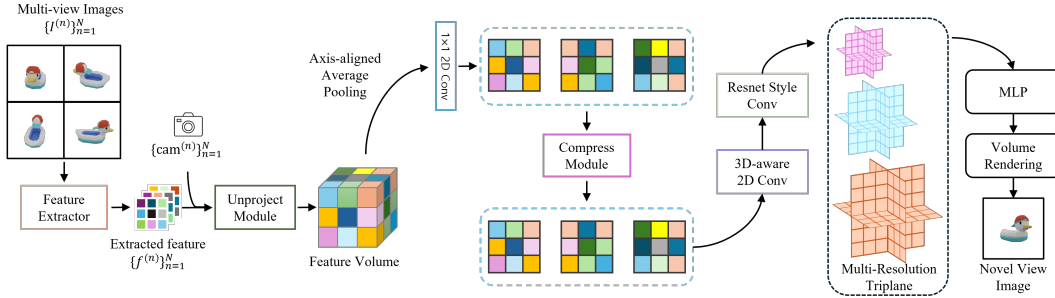


Figure 1: CodecNeRF encoder and decoder architecture. See (Section 3.1) for details

2 Related works

Fast training NeRF. Addressing the training time problem of the NeRF model has been the main focus of subsequent studies. Plenoxels [22] and DVGO [76] employ 3D grid voxel approach, saving color and density values explicitly and utilizing pruning techniques for time efficiency. TensorRF [14] used tensor decomposition on voxel grid, while Instant-NGP [55] utilized multi-voxel grid encoded through hashing indices. K-planes [21] demonstrated scalability to higher dimensions using multi-scale planes combining with EG3D’s [12] triplane method while maintaining the speed advantages of explicit 2D grid. In our approach, we also leverage multi-resolution triplanes, significantly reducing optimization time in new objects. During finetuning, the pretrained encoder and decoder remain frozen, updating only the decomposed feature tensors and LoRA weights, streamlining the process. Our method, integrating multi-resolution triplanes with pretrained initialization and efficient fine-tuning, offers a promising avenue for faster and more effective NeRF training.

Compact NeRF. Follow-up studies of NeRF aim to reduce storage size while preserving the performance of the original models. TensorRF [14] and CCNeRF [80] used tensor decomposition and low-rank approximation to reduce model size. Also, several works [22, 64] applied model pruning scheme that can be an efficient method to reduce size. Plenoxel [22] pruned the empty voxel and Masked wavelet representation [64] applied wavelet transform and trainable mask that can remove coefficients. Related to quantization methods, Re:NeRF [19] and PlenOctrees [87] used weight quantization to compress explicit voxel grid. VQRF [40] introduced trainable vector quantization method and VBNF [77] compressed feature grid by applying vector-quantized auto-decoder. We designed our neural compression techniques that suitable for parameter-efficient finetuning and achieved tremendous improvements in compression rate and also in training speed.

Neural codec for images and videos. Based on the classical rate-distortion optimization scenario studied by Shannon [69], machine learning community generated numerous data compression method. In image domain, along with CNN’s remarkable property as a feature extractor, encoder-decoder [3, 32] based methods proposed by Ballé [4, 5] are established as standard approaches. These models are combined with an entropy coding, such as [66, 52, 26], and trained to minimize the discretized code length while weighing the trade-offs between bit-rate and representation distortion. Learning-based video compression methods, expanded from image techniques, have incorporated time axis using optical flow [49], reference frames [41], and contextual learning [38, 71]. Inspired by neural compression methods in images and videos, we propose integrating neural codec into parameter-efficient finetuning of 3D representations in a novel way.

3 CodecNeRF

This section describes the proposed CodecNeRF pipeline with detailed architectures and finetuning methods. We explain the overall architecture (Section 3.1) first and present detailed methods in the following sections for each module: 3D feature construction (Section 3.2), 3D feature compression (Section 3.3), and multi-resolution triplanes (Section 3.4). Then, we present the training objectives used to train the proposed architecture (Section 3.5) and the parameter-efficient finetuning method for generating compact codes (Section 3.6 and Section 3.7).

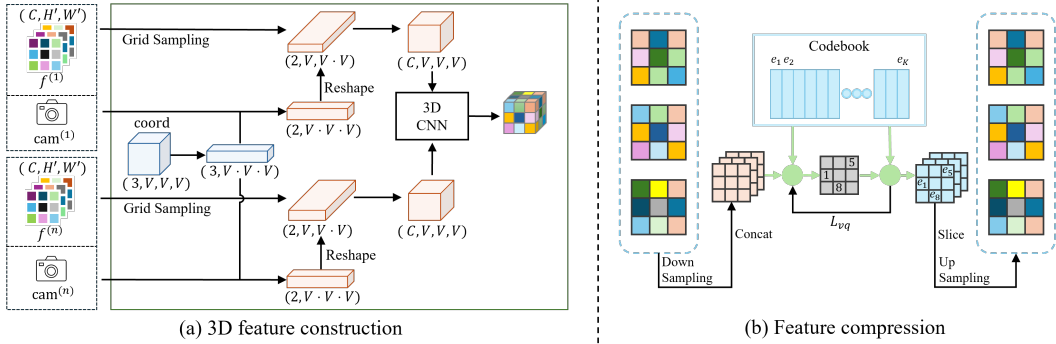


Figure 2: 3D feature construction and compression architecture. See (Section 3.2) and (Section 3.3) for details.

3.1 Overall architecture

Fig. 1 depicts the overall encoder and decoder architecture of CodecNeRF. Given N input images from different viewpoints, $\{I^{(n)}\}_{n=1}^N$, the goal is to produce a NeRF representation (multi-resolution triplanes). First, a 2D image feature extractor module, feat_θ , processes all input images and generates 2D feature maps for each input image, $\{f^{(n)}\}_{n=1}^N$. Then, the unproject and aggregation module, unproj and agg_ϕ , lifts the 2D features to 3D features and aggregates the unprojected 3D features into a single 3D feature, $f_{3D} \in \mathbb{R}^{C \times V \times V \times V}$, respectively (to avoid clutter notation, we assume height, width, and depth resolutions are same, V). The 3D feature, f_{3D} , is further processed by axis-aligned average pooling along each axis, resulting in three 2D features (a 2D feature for each axis), $f_{xy}, f_{yz}, f_{xz} \in \mathbb{R}^{C \times V \times V}$. These 2D features are used to generate multi-resolution triplanes by triplane_ψ , and finally, we perform the volumetric rendering to render an image using MLP_w . Furthermore, 2D features f_{xy}, f_{yz} , and f_{xz} are compressed by the compression module, comp_χ , producing the minimal sizes of the codes to be transmitted. The entire pipeline is differentiable, and we train end-to-end to optimize all learnable parameters, $\{\theta, \phi, \chi, \psi, \omega\}$.

3.2 3D feature construction from multi-view images

In this submodule, we construct the 3D feature from multi-view input images. To extract 2D image features, we adopt a widely known CNN architecture using feature pyramid [43], producing an image features $f^{(n)}$ given an input image $I^{(n)}$. We process each view image individually using the shared feature extractor, feat_θ . Following the conventional NeRF training scheme, we assume that we can obtain camera poses for input view images beforehand. The 3D feature construction can be written as follows.

$$f_{3D} = \text{agg}_\phi(\{\text{unproj}(f^{(n)}, \text{cam}^{(n)}, \text{coord})\}_{n=1}^N), \quad (1)$$

where $\text{cam}^{(n)}$ denotes the camera pose for the input views. Inspired by the recent unprojection methods [47, 46], we first construct a 3D coordinate tensor, $\text{coord} \in \mathbb{R}^{3 \times V \times V \times V}$, whose resolution is V for all axis. Then, each coordinate is projected into 2D space given the camera pose, and the feature is extracted from the image feature $f^{(n)}$ using bilinear interpolation, generating the intermediate 3D feature. We use an aggregation module agg_ϕ parameterized ϕ to combine N intermediate 3D features and produce the final 3D feature, $f_{3D} \in \mathbb{R}^{C \times V \times V \times V}$. We use a few 3D convolution layers to aggregate features and further extract useful information.

3.3 3D feature compression

The goal of 3D feature compression is to minimize the number of bits required to reconstruct the final NeRF representations, and f_{3D} from the previous stage is 3D volume, thus inefficient for storage and transmission purposes. In this work, we opt to use explicit-implicit hybrid NeRF representation, triplane [12]. Triplane representation decomposes a 3D volume into three 2D planes, serving as a

prevalent technique for the NeRF representations [21, 10, 73]. It scales with $O(V^2)$ for the resolution V as opposed to $O(V^3)$ for a dense 3D volume.

We first transform the 3D feature into three 2D features by average pooling along each axis.

$$f_{xy} = \text{avgpool-}z(f_{3D}), f_{yz} = \text{avgpool-}x(f_{3D}), f_{xz} = \text{avgpool-}y(f_{3D}), \quad (2)$$

where $\text{avgpool-}x$ means average pooling along x axis. Then, comp_χ compresses the three 2D feature maps using vector quantization methods [23, 59]. It consists of a downsampling CNN, an upsampling CNN, and a codebook (χ includes all parameters in these three modules). First the downsampling 2D CNN module process each 2D feature map to generate low-resolution 2D feature map, $l_{xy}, l_{yz}, l_{xz} \in \mathbb{R}^{C' \times V' \times V'} (C' \ll C \text{ and } V' \ll V)$. Then, we find the closest code from the codebook to perform the vector quantization.

$$k^* = \underset{k}{\operatorname{argmin}} \|l_{xy,i,j} - e_k\|_2, \quad (3)$$

where $e \in \mathbb{R}^{K \times C'}$ is the codebook, K is the codebook size, $e_k \in \mathbb{R}^{C'}$ denotes the k -th element of the codebook, $k^* \in \{1, \dots, K\}$ is the founded index, and $l_{xy,i,j} \in \mathbb{R}^{C'}$ denotes the element of l_{xy} indexed by (i, j) location. During training, we optimize the codebook e , and the loss function for a training instance can be written as,

$$\mathcal{L}_{\text{vq}} = \|\text{sg}[l] - e^*\|_2^2 + \lambda_{\text{commit}} \|\text{sg}[e^*] - l\|_2^2, \quad (4)$$

where $\text{sg}[\cdot]$ is the stop-gradient operator, and λ_{commit} regulate the commitment to codebook embedding. With the slight abuse of notation, here we define $l \in \mathbb{R}^{3 \times C' \times V' \times V'}$ as the concatenated tensor of three low-resolution 2D feature maps, and $e^* \in \mathbb{R}^{3 \times C' \times V' \times V'}$ is the collection of the codes we extract from the codebook for all three feature maps using Eq. (3). Finally, the upsampling CNN produces three 2D feature maps with the increased resolutions, $\bar{f}_{xy}, \bar{f}_{yz}, \bar{f}_{xz} \in \mathbb{R}^{C \times V \times V}$. During training, the input to the upsampling CNN is l , but e^* is used for the inputs during testing.

3.4 Multi-resolution triplanes

The previous works [55, 21, 44, 35, 25, 58] have shown that using a multi-resolution representation efficiently encodes spatial features at different scales. It encourages spatial smoothness across different scales, superior convergence, and better accuracy. Building upon these observations, employing different spatial resolutions would help reduce the number of features stored at the highest resolution, thus allowing for additional compression of our model. Given this motivation, we propose a hierarchical 3D-aware convolution block, triplane_ψ , that generates a multi-resolution triplane revised from the one introduced in [84]. It introduces rolled-out tri-planes that attend to all components from the relevant rows and columns, enabling cross-plane feature interaction.

$$(\tilde{f}_{xy}, \tilde{f}_{yz}, \tilde{f}_{xz}) = \text{triplane}_\psi(\bar{f}_{xy}, \bar{f}_{yz}, \bar{f}_{xz}), \quad (5)$$

where $\tilde{f}_{xy} = \{\tilde{f}_{xy}^1, \tilde{f}_{xy}^2, \tilde{f}_{xy}^3\}$ is a set of multi-resolution triplane features for ‘xy’ plane, and $\tilde{f}_{xy}^1 \in \mathbb{R}^{C \times V_1 \times V_1}$, $\tilde{f}_{xy}^2 \in \mathbb{R}^{C \times V_2 \times V_2}$, and $\tilde{f}_{xy}^3 \in \mathbb{R}^{C \times V_3 \times V_3}$ are different resolution features.

The proposed triplane renderer consists of two distinct MLP heads, coarse and fine, for decoding the RGBs and densities. Given a 3D coordinate $p \in \mathbb{R}^3$, the decoder collects the tri-plane features at three axis-aligned projected locations of $p_{xy}, p_{yz}, p_{xz} \in \mathbb{R}^2$, using bilinear interpolation. We simply concat the tri-plane features across the different scales and aggregate by summation.

$$f_{\text{tri}}(p) = \sum_{k \in \{xy, yz, xz\}} \text{concat}(\text{intp}(\tilde{f}_k^1, p_k), \text{intp}(\tilde{f}_k^2, p_k), \text{intp}(\tilde{f}_k^3, p_k)), \quad (6)$$

$$c(p), \sigma(p) = \text{MLP}_\omega(f_{\text{tri}}(p), p, \text{PE}(d)), \quad (7)$$

where $\text{intp}(\cdot, \cdot)$ bilinearly interpolates the features given the projected 2D coordinates, $\text{concat}(\cdot)$ concatenate the interpolated features, $f_{\text{tri}}(p) \in \mathbb{R}^{3C}$ is the feature to be processed by an MLP network to generate $c(p)$ and $\sigma(p)$, the color and density of a point. $\text{PE}(d)$ is the view direction after applying the positional encoding. Finally, the volume rendering [53] is applied to render the images using the two-pass hierarchical importance sampling method proposed by [54].

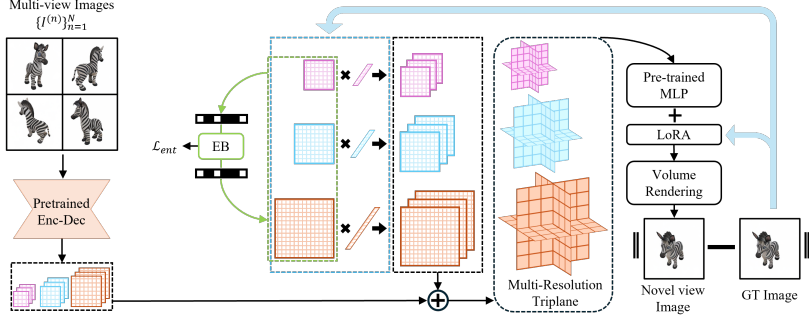


Figure 3: Parameter-efficient finetuning. See (Section 3.6) for details.

3.5 Training objective

Here, we train our base model in an end-to-end manner with its fully differentiable properties. We use L2 loss, denoted as \mathcal{L}_{rgb} to measure the pixel-wise difference between the ground truth images and rendered images.

Spatial total variation (TV) regularization encourages the sparse or smooth gradient, thereby ensuring that the feature planes do not contain erroneous high-frequency data [21, 14, 73]. We use the standard L2 TV regularization as default to make the distribution of the triplane features smoother, as it regularizes the squared difference between the neighboring values in the feature maps.

$$\mathcal{L}_{\text{tv}} = \frac{1}{T} \sum_{k \in \{xy, yz, xz\}} \sum_{s=1}^3 \sum_{i,j} \left(\left\| \tilde{f}_{k,i,j}^s - \tilde{f}_{k,i-1,j}^s \right\|_2^2 + \left\| \tilde{f}_{k,i,j}^s - \tilde{f}_{k,i,j-1}^s \right\|_2^2 \right), \quad (8)$$

where $T = 3C(V_1^2 + V_2^2 + V_3^2)$ is the total number of features across all triplanes and resolutions. The final objective function for a training instance can be written as follows,

$$\mathcal{L} = \mathcal{L}_{\text{rgb}} + \mathcal{L}_{\text{vq}} + \lambda_{\text{tv}} \mathcal{L}_{\text{tv}}. \quad (9)$$

3.6 Parameter-efficient finetuning

While the NeRF representations generated by the encoder and decoder modules are of high quality, their generalization performance on a new scene can be limited. Similar to other NeRF generalization models [79, 7], our approach can also leverage finetuning of NeRF representations to enhance visual quality for new scenes during testing time. However, effective model finetuning is severely hindered by the growing computational costs and memory storage as the model size increases. To tackle this issue, LoRA [24] is a widely used parameter-efficient finetuning (PEFT) method for adaptation of large-scale models, mainly explored in NLP and computer vision domains. LoRA has shown that only training adapter can achieve promising performance, on par with or better than the full finetuning. Thus, we propose to adapt PEFT in our test time optimization, and to the best of our knowledge, we are the first to apply PEFT to 3D NeRF representation. We first generate multi-resolution triplanes using multi-view test images, and train only the triplanes and decoder in a efficient way.

Parameter efficient triplane finetuning. We propose a tensor factorization scheme to efficiently finetune triplane representation. Let $\tilde{f}_k^s \in \mathbb{R}^{C \times V_s \times V_s}$ be the triplanes generated by the encoder and decoder for a scale ‘ s ’ and plane ‘ k ’ ($s \in \{1, 2, 3\}$ and $k \in \{xy, yz, xz\}$). The final triplane representations are expressed by $\tilde{f}_k^s + \Delta \tilde{f}_k^s$, and $\Delta \tilde{f}_k^s \in \mathbb{R}^{C \times V_s \times V_s}$ is constructed by a tensor product between matrices and vectors.

$$\Delta \tilde{f}_k^s = \sum_{r=1}^R v_r^s \circ M_{k,r}^s, \quad (10)$$

where $M_{k,r}^s \in \mathbb{R}^{V_s \times V_s}$ denotes r -th matrix for the ‘ k ’ plane and scale ‘ s ’, $v_r^s \in \mathbb{R}^C$ is the r -th vector for all three planes and scale ‘ s ’, and $\circ : \mathbb{R}^C \times \mathbb{R}^{V_s \times V_s} \rightarrow \mathbb{R}^{C \times V_s \times V_s}$ is a tensor product. During finetuning, we freeze \tilde{f}_k^s and only updates $\Delta \tilde{f}_k^s$. We apply this scheme for every feature planes in

multi-resolution triplanes and used $R = 1$ for higher compression rates (for ablation studies over different decomposition methods, please refer to the supplementary materials). For initialization, we use a common technique, setting all matrices to random values and all vectors to zeros. It makes our delta to be zero at the start of the training.

Parameter efficient MLP finetuning with LoRA. Additionally, we factorize linear layers in decoder MLP using LoRA method for MLP finetuning. Using two PEFT methods, we can achieve massive reductions in trainable parameters during test time optimization (Fig. 3). The training objective is same with the base model except for the vector quantization loss.

3.7 Entropy coding finetuning deltas

We leverage neural compression methods that have demonstrated efficacy in image and video domains to seek to achieve the optimal compression rate [4, 5, 38, 41, 71]. We adopt a fully factorized density model [5] to our proposed parameter-efficient finetuning of the triplanes. We model the prior using a non-parametric density, which is convolved with a standard uniform density in a differentiable manner (please refer to [5] for more details). Then, our training objective is defined as follows.

$$\mathcal{L}_{\text{ent}} = \sum_{k \in \{xy, yz, xz\}} \sum_{r=1}^R \sum_{s=1}^3 -\log p(M_{k,r}^s), \quad (11)$$

$$\mathcal{L} = \mathcal{L}_{\text{rgb}} + \lambda_{\text{rate}} \mathcal{L}_{\text{ent}} + \lambda_{\text{tv}} \mathcal{L}_{\text{tv}}, \quad (12)$$

where λ_{rate} will balance between the quantization error and the code length. We only applied the entropy model to the feature matrices for triplane features, and after finetuning, updated matrices $M_{k,r}^s$ are quantized and compressed, while other weights, $\omega_a, \omega_b, v_r^s$ are stored with 32-bit precision as a convention. Please see the supplementary for the details and entropy coding on MLP (LoRA).

4 Experiments

4.1 Datasets

To evaluate our method, we conduct experiments on 1) ShapeNet [13] for category-specific view synthesis, 2) Objaverse [18] for category-agnostic view synthesis, and 3) DTU MVS dataset [28] for real scenes. In ShapeNet, we selected ‘car’ and ‘chair’ classes with 224×224 image resolution, and used the same training/testing split in DISN [86]. For Objaverse, we sourced images from One-2-3-45 [46], which consists of 46k 3D objects, and constructed our own split of 36,796 training objects and 9,118 test objects. Lastly, we follow PixelNeRF [88] DTU dataset split with 88 scenes for training and 15 scenes for testing. Images are rendered at a resolution of 256×256 in Objaverse and DTU datasets.

4.2 Implementation Details

To train our base model, we randomly choose 16 input images and camera poses to produce a triplane representation and predict the remaining novel views. In the finetuning stage, we first generated an initial representation using predetermined 16 view indices and trained the triplane feature with

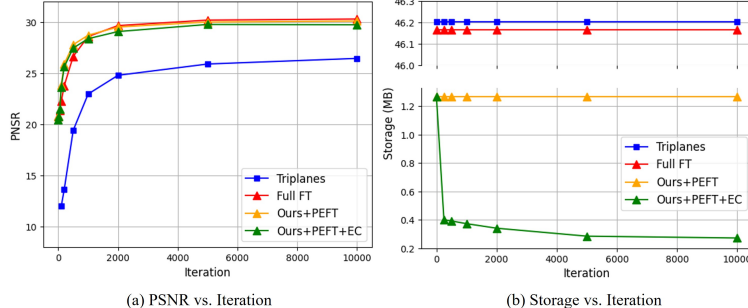


Figure 4: Comparison of optimization speed and compression degrees.

an MLP decoder in an optimization-based approach. We finetune the model using 24 images and then test it on the remaining views. Note that the 16 images used to generate the initial triplane representations are a subset of the 24 training images and the same images are all used to train baseline models for a fair comparison. For DTU dataset, we choose 8 images for training, and 16 images for finetuning. We set the LoRA’s rank to 4 and connected it to every layer in the decoder. Different rank sizes showed a trade-off between compactness and quality. Please see the supplementary for the more details and ablation study.

4.3 Results

Object-level Benchmarks. To assess the efficacy of our method in test time optimization, we employ K-planes [21] as our baseline model, which has shown fast training and compact representation. We revised the architecture based on our method for a fair comparison, and this model will be referred to as ‘Triplanes’. We evaluated the performance under three different scenarios starting from our generated triplane initializations: 1) full finetuning, 2) parameter-efficient finetuning, and 3) parameter-efficient finetuning with the proposed entropy coding.

Table 1: Compression performance.

Component	Total size in MB (codes + finetuning deltas)				
	Triplanes	Full FT	PEFT	PEFT++	W/O FT
Codebook	.	0.003	0.003	0.003	0.003
Feature	33.03	33.03	1.033	0.036	.
MLP	13.173	13.132	0.233	0.233	.
Total	46.203	46.165	1.269	0.272	0.003

Table 2: The rendered image quality.

Component	Triplanes	CodecNeRF			
		(Full FT)	(PEFT)	(PEFT++)	(w/o FT)
Obj	27.44	30.34	30.05	30.12	21.85
Car	29.51	30.51	29.51	30.37	23.52
Chair	31.54	35.17	35.47	35.66	21.19

Table 3: Quantitative results of the proposed methods evaluated on ShapeNet car, chair categories, and Objaverse datasets (denoted by ‘Obj’). ‘Full FT’ denotes full finetuning, ‘PEFT++’ denotes parameter efficient finetuning with entropy coding, and ‘MSIM’ is MSSSIM.

Data	Method	Iteration											
		0			500			1000			2000		
		PSNR	SSIM	MSIM	PSNR	SSIM	MSIM	PSNR	SSIM	MSIM	PSNR	SSIM	MSIM
Car	Triplanes	8.33	0.703	0.221	25.93	0.916	0.952	26.80	0.930	0.942	28.39	0.949	0.974
	CodecNeRF (PEFT)	23.52	0.880	0.922	29.06	0.941	0.977	29.96	0.952	0.981	30.46	0.958	0.981
	CodecNeRF (PEFT++)	.	.	.	28.91	0.939	0.976	29.81	0.950	0.980	30.36	0.956	0.982
Chair	Triplanes	8.36	0.729	0.250	24.11	0.906	0.872	27.69	0.945	0.957	29.62	0.960	0.970
	CodecNeRF (PEFT)	21.19	0.877	0.867	32.65	0.972	0.988	33.84	0.978	0.991	34.57	0.982	0.992
	CodecNeRF (PEFT++)	.	.	.	32.21	0.969	0.987	33.52	0.977	0.991	34.32	0.982	0.992
Obj	Triplanes	11.44	0.788	0.352	21.58	0.852	0.855	24.43	0.896	0.926	26.06	0.918	0.950
	CodecNeRF (PEFT)	21.85	0.852	0.865	28.48	0.929	0.967	29.20	0.939	0.973	29.76	0.946	0.978
	CodecNeRF (PEFT++)	.	.	.	28.16	0.926	0.965	28.92	0.935	0.971	29.45	0.943	0.975

Table 1 and Table 2 shows the component level storage comparison (on Objaverse dataset) and rendered image quality, after trained with 10k iterations. Our method can store and transmit the 3D representation ($150\times$ compactness) with better quality compared to the baseline model. The qualitative results in Table 3 and Fig. 4 (a), our method shows fast encoding progress from its initialized representation and improvement on all metrics (measured in PSNR, SSIM, and MS-SSIM). Also, in Fig. 4 (b), we plot the storage requirement that the receiver can perfectly restore the encoded representation. Due to the improved generalization capability of our method, we outperform the per-scene optimization-based baseline. Triplanes, in novel view synthesis. Remarkably, the PEFT method showed comparable or better performance across the data with fewer trainable parameters. The qualitative results in Fig. 6 presents the novel view synthesis results across the finetuning iteration, illustrating the generalization ability and fast encoding speed of our methods.

Scene-level Benchmarks. We further demonstrate the applicability of our method to real scenes using the DTU datasets. Our method, CodecNeRF, is compared with representative optimization-based methods, TensoRF [14] and 3D-GS [31], as shown in Table 4. As previously stated, we utilized 16 training images and tested on the remaining views. Our method was trained for less than a minute to evaluate its fast encoding ability. Fig. 7 presents the novel view synthesis results on the DTU datasets. Both quantitative and qualitative results indicate that our method surpasses TensoRF and 3D-GS in terms of quality, even with a compact representation. Please refer to the supplementary material for additional examples and detailed training configuration.

Table 4: Performance comparison on DTU datasets.

Method		PSNR	SSIM	Train (s)	Size (MB)
TensoRF	Mean	16.48	0.597	235.3	24.05
	SD	1.83	0.13	12.76	0.086
3D-GS	Mean	15.77	0.58	64.0	156.9
	SD	2.25	0.142	6.23	123.59
Ours (PEFT)	Mean	20.15	0.667	36.4	0.89
	SD	2.29	0.116	1.35	0.038
Ours (PEFT++)	Mean	18.45	0.567	58.9	0.403
	SD	1.84	0.097	1.99	0.002

In-depth Evaluations. We conducted a detailed comparison of our model with both fast and compact specialized methods using the Objaverse dataset [18]. For fast training NeRF, we adopted TensoRF [14] and DVGO [76], and for compact NeRF, we utilized VQRF [40] and MaskDWT [64]. As illustrated in Fig. 5, our method demonstrates the ability to achieve fast encoding and a high compression ratio, outperforming each representative model in both aspects.

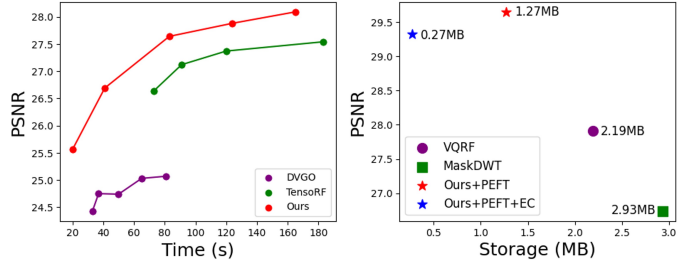


Figure 5: In-depth evaluations.

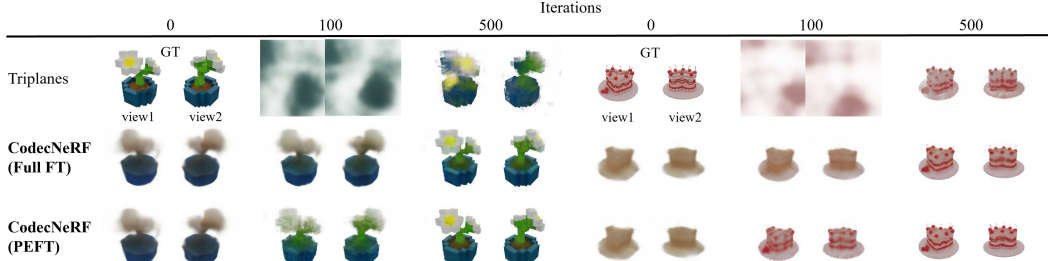


Figure 6: Novel view synthesis results on Objaverse dataset.

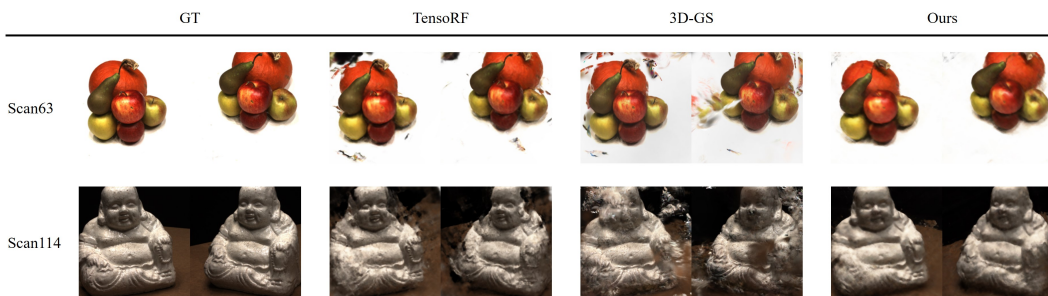


Figure 7: Novel view synthesis results on DTU MVS dataset.

Feature Visualization We also visualized the delta feature maps across finetuning iterations based on our entropy coding method. As shown in Fig. 8, the feature maps following the entropy coding, eliminate unnecessary components across the different resolutions, and get a high compression ratio resulting from quantization. This observation aligns with our intuition that employing different spatial resolutions would help reduce the quantity of information stored at each resolution, thus making the use of entropy models as an ideal strategy.

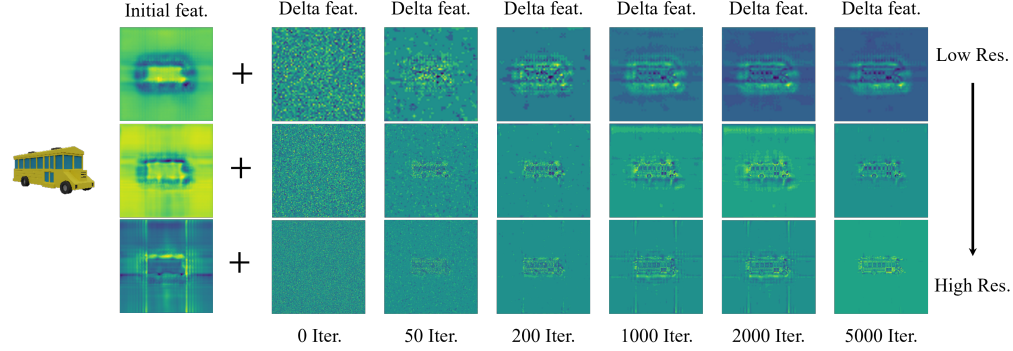


Figure 8: Visualization of delta feature maps trained with entropy coding. The averaged YZ planes across the channel dimensions are shown in the different resolutions.

5 Limitations and Future Works

While CodecNeRF demonstrates promising performance in terms of fast encoding speed and compression ratio, it is important to acknowledge that the current framework still possesses limitations. First, further technical advancements are essential to encode more complicated scenes and objects, such as large-scale scenes (e.g., Mip-NeRF 360 datasets). Block-wise or hierarchical codings are promising directions to be explored, and training on large 3D scenes or videos could enhance the adaptability of CodecNeRF for such scenarios. Second, to support other NeRF representations, including instant NGP or 3D Gaussian Splatting, it will require modifications to the current architecture and training algorithms, potentially involving a point-based neural encoder and decoder. To further improve the rendering quality and encoding speed, we may consider investigating the utilization of larger encoder and decoder architectures and incorporating learned 2D priors [68, 60] as a form of supervision. Lastly, we can utilize advanced techniques in neural codecs or weight-pruning methods to optimize compression performance.

6 Conclusion

In this work, we introduced CodecNeRF, a novel encoding-decoding-finetuning pipeline designed for fast encoding and decoding, compact codes, and high-quality renderings. Our experimental results demonstrated a significant performance improvement over a strong NeRF baseline model across commonly used 3D object datasets, including ShapeNet and Objaverse, as well as the scene-level DTU MVS dataset. We believe that our framework has a potential to pave the way for new research directions and broaden the applications of NeRF. Our work provides compelling evidence that 3D representations can be encoded with efficiency comparable to that of traditional image and video data.

References

- [1] Adamkiewicz, M., Chen, T., Caccavale, A., Gardner, R., Culbertson, P., Bohg, J., Schwager, M.: Vision-only robot navigation in a neural radiance world. *IEEE Robotics and Automation Letters* **7**(2), 4606–4613 (2022)
- [2] Baatz, H., Granskog, J., Papas, M., Rousselle, F., Novák, J.: Nerf-tex: Neural reflectance field textures. In: *Computer Graphics Forum*. vol. 41, pp. 287–301. Wiley Online Library (2022)
- [3] Baldi, P.: Autoencoders, unsupervised learning, and deep architectures. In: *Proceedings of ICML workshop on unsupervised and transfer learning*. pp. 37–49. JMLR Workshop and Conference Proceedings (2012)
- [4] Ballé, J., Laparra, V., Simoncelli, E.P.: End-to-end optimized image compression. arXiv preprint arXiv:1611.01704 (2016)
- [5] Ballé, J., Minnen, D., Singh, S., Hwang, S.J., Johnston, N.: Variational image compression with a scale hyperprior. arXiv preprint arXiv:1802.01436 (2018)
- [6] Barron, J.T., Mildenhall, B., Verbin, D., Srinivasan, P.P., Hedman, P.: Mip-nerf 360: Unbounded anti-aliased neural radiance fields. In: *Proceedings of the IEEE/CVF Conference on Computer Vision and Pattern Recognition*. pp. 5470–5479 (2022)
- [7] Bergman, A., Kellnhofer, P., Wetzstein, G.: Fast training of neural lumigraph representations using meta learning. *Advances in Neural Information Processing Systems* **34**, 172–186 (2021)
- [8] Bird, T., Ballé, J., Singh, S., Chou, P.A.: 3d scene compression through entropy penalized neural representation functions. In: *2021 Picture Coding Symposium (PCS)*. pp. 1–5. IEEE (2021)
- [9] Bross, B., Wang, Y.K., Ye, Y., Liu, S., Chen, J., Sullivan, G.J., Ohm, J.R.: Overview of the versatile video coding (vvvc) standard and its applications. *IEEE Transactions on Circuits and Systems for Video Technology* **31**(10), 3736–3764 (2021)
- [10] Cao, A., Johnson, J.: Hexplane: A fast representation for dynamic scenes. *CVPR* (2023)
- [11] Caron, M., Touvron, H., Misra, I., Jégou, H., Mairal, J., Bojanowski, P., Joulin, A.: Emerging properties in self-supervised vision transformers. In: *Proceedings of the IEEE/CVF international conference on computer vision*. pp. 9650–9660 (2021)
- [12] Chan, E.R., Lin, C.Z., Chan, M.A., Nagano, K., Pan, B., Mello, S.D., Gallo, O., Guibas, L., Tremblay, J., Khamis, S., Karras, T., Wetzstein, G.: Efficient geometry-aware 3d generative adversarial networks (2022)
- [13] Chang, A.X., Funkhouser, T., Guibas, L., Hanrahan, P., Huang, Q., Li, Z., Savarese, S., Savva, M., Song, S., Su, H., et al.: Shapenet: An information-rich 3d model repository. arXiv preprint arXiv:1512.03012 (2015)
- [14] Chen, A., Xu, Z., Geiger, A., Yu, J., Su, H.: Tensorf: Tensorial radiance fields. In: *Computer Vision–ECCV 2022: 17th European Conference, Tel Aviv, Israel, October 23–27, 2022, Proceedings, Part XXXII*. pp. 333–350. Springer (2022)
- [15] Chen, A., Xu, Z., Zhao, F., Zhang, X., Xiang, F., Yu, J., Su, H.: Mvsnerf: Fast generalizable radiance field reconstruction from multi-view stereo. In: *Proceedings of the IEEE/CVF International Conference on Computer Vision*. pp. 14124–14133 (2021)
- [16] Chibane, J., Bansal, A., Lazova, V., Pons-Moll, G.: Stereo radiance fields (srf): Learning view synthesis for sparse views of novel scenes. In: *Proceedings of the IEEE/CVF Conference on Computer Vision and Pattern Recognition*. pp. 7911–7920 (2021)
- [17] Deitke, M., Liu, R., Wallingford, M., Ngo, H., Michel, O., Kusupati, A., Fan, A., Laforte, C., Voleti, V., Gadre, S.Y., et al.: Objaverse-xl: A universe of 10m+ 3d objects. *Advances in Neural Information Processing Systems* **36** (2024)

- [18] Deitke, M., Schwenk, D., Salvador, J., Weihs, L., Michel, O., VanderBilt, E., Schmidt, L., Ehsani, K., Kembhavi, A., Farhadi, A.: Objaverse: A universe of annotated 3d objects. In: Proceedings of the IEEE/CVF Conference on Computer Vision and Pattern Recognition. pp. 13142–13153 (2023)
- [19] Deng, C.L., Tartaglione, E.: Compressing explicit voxel grid representations: fast nerfs become also small. In: Proceedings of the IEEE/CVF Winter Conference on Applications of Computer Vision. pp. 1236–1245 (2023)
- [20] Dupont, E., Martin, M.B., Colburn, A., Sankar, A., Susskind, J., Shan, Q.: Equivariant neural rendering. In: International Conference on Machine Learning. pp. 2761–2770. PMLR (2020)
- [21] Fridovich-Keil, S., Meanti, G., Warburg, F.R., Recht, B., Kanazawa, A.: K-planes: Explicit radiance fields in space, time, and appearance. In: CVPR (2023)
- [22] Fridovich-Keil, S., Yu, A., Tancik, M., Chen, Q., Recht, B., Kanazawa, A.: Plenoxels: Radiance fields without neural networks. In: Proceedings of the IEEE/CVF Conference on Computer Vision and Pattern Recognition. pp. 5501–5510 (2022)
- [23] Gray, R.: Vector quantization. IEEE ASSP Magazine **1**(2), 4–29 (1984)
- [24] Hu, E.J., Shen, Y., Wallis, P., Allen-Zhu, Z., Li, Y., Wang, S., Wang, L., Chen, W.: Lora: Low-rank adaptation of large language models. arXiv preprint arXiv:2106.09685 (2021)
- [25] Hu, W., Wang, Y., Ma, L., Yang, B., Gao, L., Liu, X., Ma, Y.: Tri-miprf: Tri-mip representation for efficient anti-aliasing neural radiance fields. In: Proceedings of the IEEE/CVF International Conference on Computer Vision. pp. 19774–19783 (2023)
- [26] Huffman, D.A.: A method for the construction of minimum-redundancy codes. Proceedings of the IRE **40**(9), 1098–1101 (1952)
- [27] Jampani, V., Chang, H., Sargent, K., Kar, A., Tucker, R., Krainin, M., Kaeser, D., Freeman, W.T., Salesin, D., Curless, B., et al.: Slide: Single image 3d photography with soft layering and depth-aware inpainting. In: Proceedings of the IEEE/CVF International Conference on Computer Vision. pp. 12518–12527 (2021)
- [28] Jensen, R., Dahl, A., Vogiatzis, G., Tola, E., Aanæs, H.: Large scale multi-view stereopsis evaluation. In: Proceedings of the IEEE conference on computer vision and pattern recognition. pp. 406–413 (2014)
- [29] Johari, M.M., Lepoittevin, Y., Fleuret, F.: Geonerf: Generalizing nerf with geometry priors. In: Proceedings of the IEEE/CVF Conference on Computer Vision and Pattern Recognition. pp. 18365–18375 (2022)
- [30] Kato, H., Ushiku, Y., Harada, T.: Neural 3d mesh renderer. In: Proceedings of the IEEE conference on computer vision and pattern recognition. pp. 3907–3916 (2018)
- [31] Kerbl, B., Kopanas, G., Leimkühler, T., Drettakis, G.: 3d gaussian splatting for real-time radiance field rendering. ACM Transactions on Graphics **42**(4) (2023)
- [32] Kingma, D.P., Welling, M.: Auto-encoding variational bayes. arXiv preprint arXiv:1312.6114 (2013)
- [33] Kuang, Z., Luan, F., Bi, S., Shu, Z., Wetzstein, G., Sunkavalli, K.: Palettenerf: Palette-based appearance editing of neural radiance fields. In: Proceedings of the IEEE/CVF Conference on Computer Vision and Pattern Recognition. pp. 20691–20700 (2023)
- [34] Kuang, Z., Olszewski, K., Chai, M., Huang, Z., Achlioptas, P., Tulyakov, S.: Neroic: Neural rendering of objects from online image collections. ACM Transactions on Graphics (TOG) **41**(4), 1–12 (2022)
- [35] Kuznetsov, A.: Neumip: Multi-resolution neural materials. ACM Transactions on Graphics (TOG) **40**(4) (2021)

- [36] Kwon, O., Park, J., Oh, S.: Renderable neural radiance map for visual navigation. In: Proceedings of the IEEE/CVF Conference on Computer Vision and Pattern Recognition. pp. 9099–9108 (2023)
- [37] Lee, J.C., Rho, D., Sun, X., Ko, J.H., Park, E.: Compact 3d gaussian representation for radiance field. arXiv preprint arXiv:2311.13681 (2023)
- [38] Li, J., Li, B., Lu, Y.: Deep contextual video compression. Advances in Neural Information Processing Systems **34**, 18114–18125 (2021)
- [39] Li, J., Feng, Z., She, Q., Ding, H., Wang, C., Lee, G.H.: Mine: Towards continuous depth mpi with nerf for novel view synthesis. In: Proceedings of the IEEE/CVF International Conference on Computer Vision. pp. 12578–12588 (2021)
- [40] Li, L., Shen, Z., Wang, Z., Shen, L., Bo, L.: Compressing volumetric radiance fields to 1 mb. In: Proceedings of the IEEE/CVF Conference on Computer Vision and Pattern Recognition. pp. 4222–4231 (2023)
- [41] Lin, J., Liu, D., Li, H., Wu, F.: M-lvc: Multiple frames prediction for learned video compression. In: Proceedings of the IEEE/CVF Conference on Computer Vision and Pattern Recognition. pp. 3546–3554 (2020)
- [42] Lin, K.E., Lin, Y.C., Lai, W.S., Lin, T.Y., Shih, Y.C., Ramamoorthi, R.: Vision transformer for nerf-based view synthesis from a single input image. In: Proceedings of the IEEE/CVF Winter Conference on Applications of Computer Vision. pp. 806–815 (2023)
- [43] Lin, T.Y., Dollár, P., Girshick, R., He, K., Hariharan, B., Belongie, S.: Feature pyramid networks for object detection. In: Proceedings of the IEEE conference on computer vision and pattern recognition. pp. 2117–2125 (2017)
- [44] Lindell, D.B., Van Veen, D., Park, J.J., Wetzstein, G.: Bacon: Band-limited coordinate networks for multiscale scene representation. In: Proceedings of the IEEE/CVF conference on computer vision and pattern recognition. pp. 16252–16262 (2022)
- [45] Liu, L., Gu, J., Zaw Lin, K., Chua, T.S., Theobalt, C.: Neural sparse voxel fields. Advances in Neural Information Processing Systems **33**, 15651–15663 (2020)
- [46] Liu, M., Xu, C., Jin, H., Chen, L., Varma T, M., Xu, Z., Su, H.: One-2-3-45: Any single image to 3d mesh in 45 seconds without per-shape optimization. In: Advances in Neural Information Processing Systems. vol. 36, pp. 22226–22246. Curran Associates, Inc. (2023)
- [47] Liu, Y., Lin, C., Zeng, Z., Long, X., Liu, L., Komura, T., Wang, W.: Syncdreamer: Generating multiview-consistent images from a single-view image (2023)
- [48] Liu, Y., Peng, S., Liu, L., Wang, Q., Wang, P., Theobalt, C., Zhou, X., Wang, W.: Neural rays for occlusion-aware image-based rendering. In: Proceedings of the IEEE/CVF Conference on Computer Vision and Pattern Recognition. pp. 7824–7833 (2022)
- [49] Lu, G., Ouyang, W., Xu, D., Zhang, X., Cai, C., Gao, Z.: Dvc: An end-to-end deep video compression framework. In: Proceedings of the IEEE/CVF Conference on Computer Vision and Pattern Recognition. pp. 11006–11015 (2019)
- [50] Lu, Y., Jiang, K., Levine, J.A., Berger, M.: Compressive neural representations of volumetric scalar fields. In: Computer Graphics Forum. vol. 40, pp. 135–146. Wiley Online Library (2021)
- [51] Maggio, D., Abate, M., Shi, J., Mario, C., Carbone, L.: Loc-nerf: Monte carlo localization using neural radiance fields. In: 2023 IEEE International Conference on Robotics and Automation (ICRA). pp. 4018–4025. IEEE (2023)
- [52] Martin, G.N.N.: Range encoding: an algorithm for removing redundancy from a digitised message. In: Proc. Institution of Electronic and Radio Engineers International Conference on Video and Data Recording. vol. 2 (1979)
- [53] Max, N.: Optical models for direct volume rendering. IEEE Transactions on Visualization and Computer Graphics **1**(2), 99–108 (1995)

- [54] Mildenhall, B., Srinivasan, P.P., Tancik, M., Barron, J.T., Ramamoorthi, R., Ng, R.: Nerf: Representing scenes as neural radiance fields for view synthesis. In: ECCV (2020)
- [55] Müller, T., Evans, A., Schied, C., Keller, A.: Instant neural graphics primitives with a multiresolution hash encoding. ACM Transactions on Graphics (ToG) **41**(4), 1–15 (2022)
- [56] Munkberg, J., Hasselgren, J., Shen, T., Gao, J., Chen, W., Evans, A., Müller, T., Fidler, S.: Extracting Triangular 3D Models, Materials, and Lighting From Images. In: Proceedings of the IEEE/CVF Conference on Computer Vision and Pattern Recognition (CVPR). pp. 8280–8290 (June 2022)
- [57] Munkberg, J., Hasselgren, J., Shen, T., Gao, J., Chen, W., Evans, A., Müller, T., Fidler, S.: Extracting triangular 3d models, materials, and lighting from images. In: Proceedings of the IEEE/CVF Conference on Computer Vision and Pattern Recognition. pp. 8280–8290 (2022)
- [58] Nam, S., Rho, D., Ko, J.H., Park, E.: Mip-grid: Anti-aliased grid representations for neural radiance fields. Advances in Neural Information Processing Systems **36** (2024)
- [59] van den Oord, A., Vinyals, O., kavukcuoglu, k.: Neural discrete representation learning. In: Advances in Neural Information Processing Systems. vol. 30. Curran Associates, Inc. (2017)
- [60] Radford, A., Kim, J.W., Hallacy, C., Ramesh, A., Goh, G., Agarwal, S., Sastry, G., Askell, A., Mishkin, P., Clark, J., et al.: Learning transferable visual models from natural language supervision. In: International conference on machine learning. pp. 8748–8763. PMLR (2021)
- [61] Raj, A., Zollhoefer, M., Simon, T., Saragih, J., Saito, S., Hays, J., Lombardi, S.: Pva: Pixel-aligned volumetric avatars. arXiv preprint arXiv:2101.02697 (2021)
- [62] Rakotosaona, M.J., Manhardt, F., Arroyo, D.M., Niemeyer, M., Kundu, A., Tombari, F.: Nerfmeshing: Distilling neural radiance fields into geometrically-accurate 3d meshes. arXiv preprint arXiv:2303.09431 (2023)
- [63] Rematas, K., Martin-Brualla, R., Ferrari, V.: Sharf: Shape-conditioned radiance fields from a single view. arXiv preprint arXiv:2102.08860 (2021)
- [64] Rho, D., Lee, B., Nam, S., Lee, J.C., Ko, J.H., Park, E.: Masked wavelet representation for compact neural radiance fields. In: Proceedings of the IEEE/CVF Conference on Computer Vision and Pattern Recognition. pp. 20680–20690 (2023)
- [65] Rijkse, K.: H. 263: Video coding for low-bit-rate communication. IEEE Communications magazine **34**(12), 42–45 (1996)
- [66] Rissanen, J., Langdon, G.G.: Arithmetic coding. IBM Journal of research and development **23**(2), 149–162 (1979)
- [67] Ročková, V., George, E.I.: The spike-and-slab lasso. Journal of the American Statistical Association **113**(521), 431–444 (2018)
- [68] Rombach, R., Blattmann, A., Lorenz, D., Esser, P., Ommer, B.: High-resolution image synthesis with latent diffusion models. In: Proceedings of the IEEE/CVF conference on computer vision and pattern recognition. pp. 10684–10695 (2022)
- [69] Shannon, C.E., et al.: Coding theorems for a discrete source with a fidelity criterion. IRE Nat. Conv. Rec **4**(142-163), 1 (1959)
- [70] Shen, T., Gao, J., Yin, K., Liu, M.Y., Fidler, S.: Deep marching tetrahedra: a hybrid representation for high-resolution 3d shape synthesis. Advances in Neural Information Processing Systems **34**, 6087–6101 (2021)
- [71] Sheng, X., Li, J., Li, B., Li, L., Liu, D., Lu, Y.: Temporal context mining for learned video compression. IEEE Transactions on Multimedia (2022)
- [72] Shin, S., Park, J.: Binary radiance fields. Advances in Neural Information Processing Systems **36** (2024)

- [73] Shue, J.R., Chan, E.R., Po, R., Ankner, Z., Wu, J., Wetzstein, G.: 3d neural field generation using triplane diffusion (2022)
- [74] Sitzmann, V., Zollhöfer, M., Wetzstein, G.: Scene representation networks: Continuous 3d-structure-aware neural scene representations. *Advances in Neural Information Processing Systems* **32** (2019)
- [75] Sullivan, G.J., Ohm, J.R., Han, W.J., Wiegand, T.: Overview of the high efficiency video coding (hevc) standard. *IEEE Transactions on circuits and systems for video technology* **22**(12), 1649–1668 (2012)
- [76] Sun, C., Sun, M., Chen, H.T.: Direct voxel grid optimization: Super-fast convergence for radiance fields reconstruction. In: *Proceedings of the IEEE/CVF Conference on Computer Vision and Pattern Recognition*. pp. 5459–5469 (2022)
- [77] Takikawa, T., Evans, A., Tremblay, J., Müller, T., McGuire, M., Jacobson, A., Fidler, S.: Variable bitrate neural fields. In: *ACM SIGGRAPH 2022 Conference Proceedings*. pp. 1–9 (2022)
- [78] Takikawa, T., Müller, T., Nimier-David, M., Evans, A., Fidler, S., Jacobson, A., Keller, A.: Compact neural graphics primitives with learned hash probing. In: *SIGGRAPH Asia 2023 Conference Papers*. pp. 1–10 (2023)
- [79] Tancik, M., Mildenhall, B., Wang, T., Schmidt, D., Srinivasan, P.P., Barron, J.T., Ng, R.: Learned initializations for optimizing coordinate-based neural representations. In: *Proceedings of the IEEE/CVF Conference on Computer Vision and Pattern Recognition*. pp. 2846–2855 (2021)
- [80] Tang, J., Chen, X., Wang, J., Zeng, G.: Compressible-composable nerf via rank-residual decomposition. *Advances in Neural Information Processing Systems* **35**, 14798–14809 (2022)
- [81] Tang, J., Zhou, H., Chen, X., Hu, T., Ding, E., Wang, J., Zeng, G.: Delicate textured mesh recovery from nerf via adaptive surface refinement. *arXiv preprint arXiv:2303.02091* (2023)
- [82] Trevithick, A., Yang, B.: Grf: Learning a general radiance field for 3d representation and rendering. In: *Proceedings of the IEEE/CVF International Conference on Computer Vision*. pp. 15182–15192 (2021)
- [83] Wang, Q., Wang, Z., Genova, K., Srinivasan, P.P., Zhou, H., Barron, J.T., Martin-Brualla, R., Snavely, N., Funkhouser, T.: Ibrnet: Learning multi-view image-based rendering. In: *Proceedings of the IEEE/CVF Conference on Computer Vision and Pattern Recognition*. pp. 4690–4699 (2021)
- [84] Wang, T., Zhang, B., Zhang, T., Gu, S., Bao, J., Baltrusaitis, T., Shen, J., Chen, D., Wen, F., Chen, Q., Guo, B.: Rodin: A generative model for sculpting 3d digital avatars using diffusion (2022)
- [85] Wiegand, T., Sullivan, G.J., Bjontegaard, G., Luthra, A.: Overview of the h. 264/avc video coding standard. *IEEE Transactions on circuits and systems for video technology* **13**(7), 560–576 (2003)
- [86] Xu, Q., Wang, W., Ceylan, D., Mech, R., Neumann, U.: Disn: Deep implicit surface network for high-quality single-view 3d reconstruction. *Advances in neural information processing systems* **32** (2019)
- [87] Yu, A., Li, R., Tancik, M., Li, H., Ng, R., Kanazawa, A.: Plenoctrees for real-time rendering of neural radiance fields. In: *Proceedings of the IEEE/CVF International Conference on Computer Vision*. pp. 5752–5761 (2021)
- [88] Yu, A., Ye, V., Tancik, M., Kanazawa, A.: pixelnerf: Neural radiance fields from one or few images. In: *Proceedings of the IEEE/CVF Conference on Computer Vision and Pattern Recognition*. pp. 4578–4587 (2021)

Appendix

A Additional Results

A.1 Category-agnostic: NeRF synthetic dataset

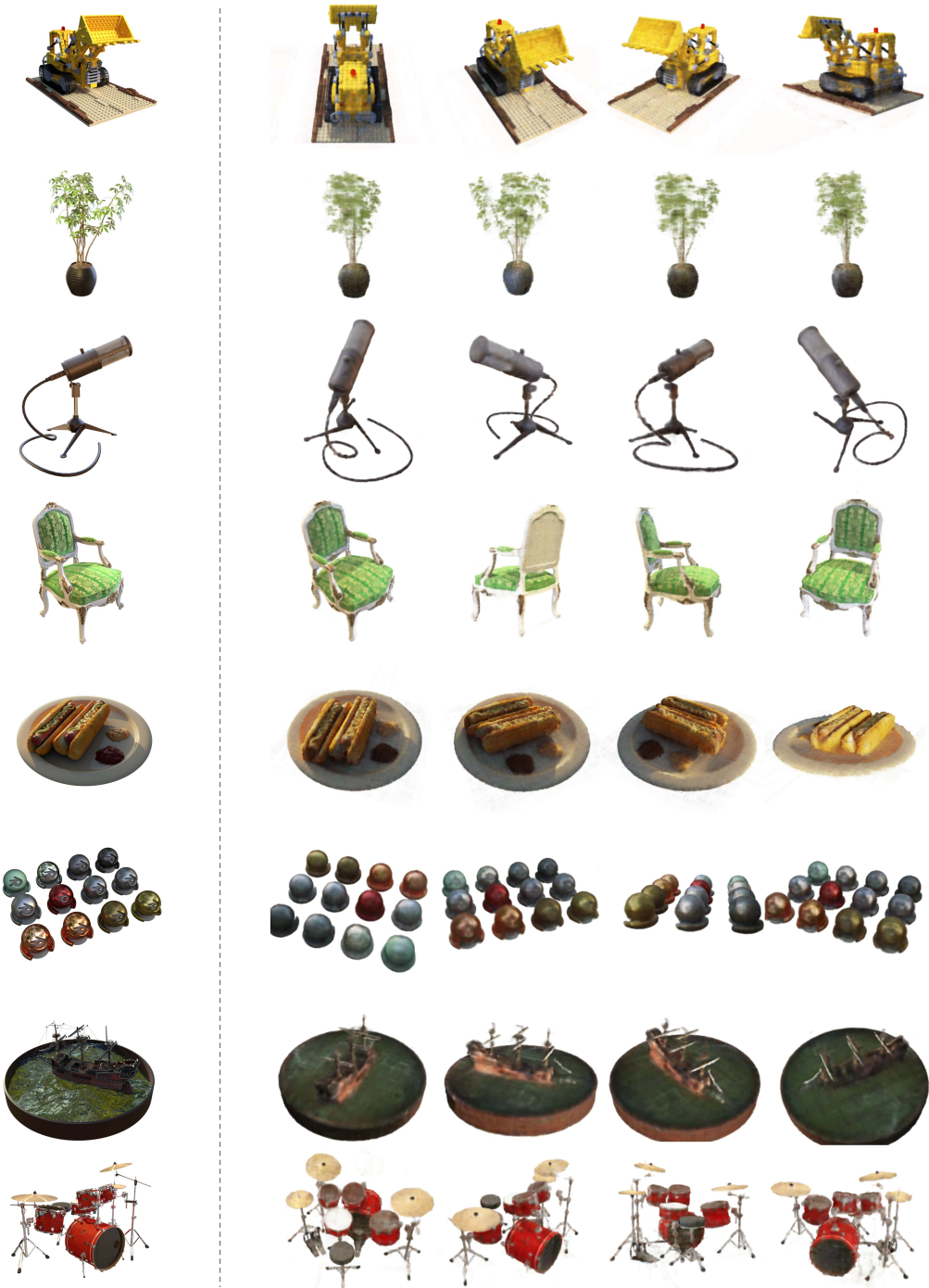


Figure 9: Novel view synthesis results on NeRF synthetic dataset

We have applied our methods using the model which was trained with the Objaverse dataset, on the NeRF synthetic dataset [54]. To accommodate the dataset to our model, we downsampled the original dataset resolution from 800×800 to 256×256 . The entire training set was utilized for finetuning, and novel views were generated to demonstrate the results. We performed finetuning over 500 iterations, with each instance taking approximately 30 seconds. The results indicate that our method exhibits rapid and robust generalization performance on complex data.

A.2 Category-agnostic: Objaverse

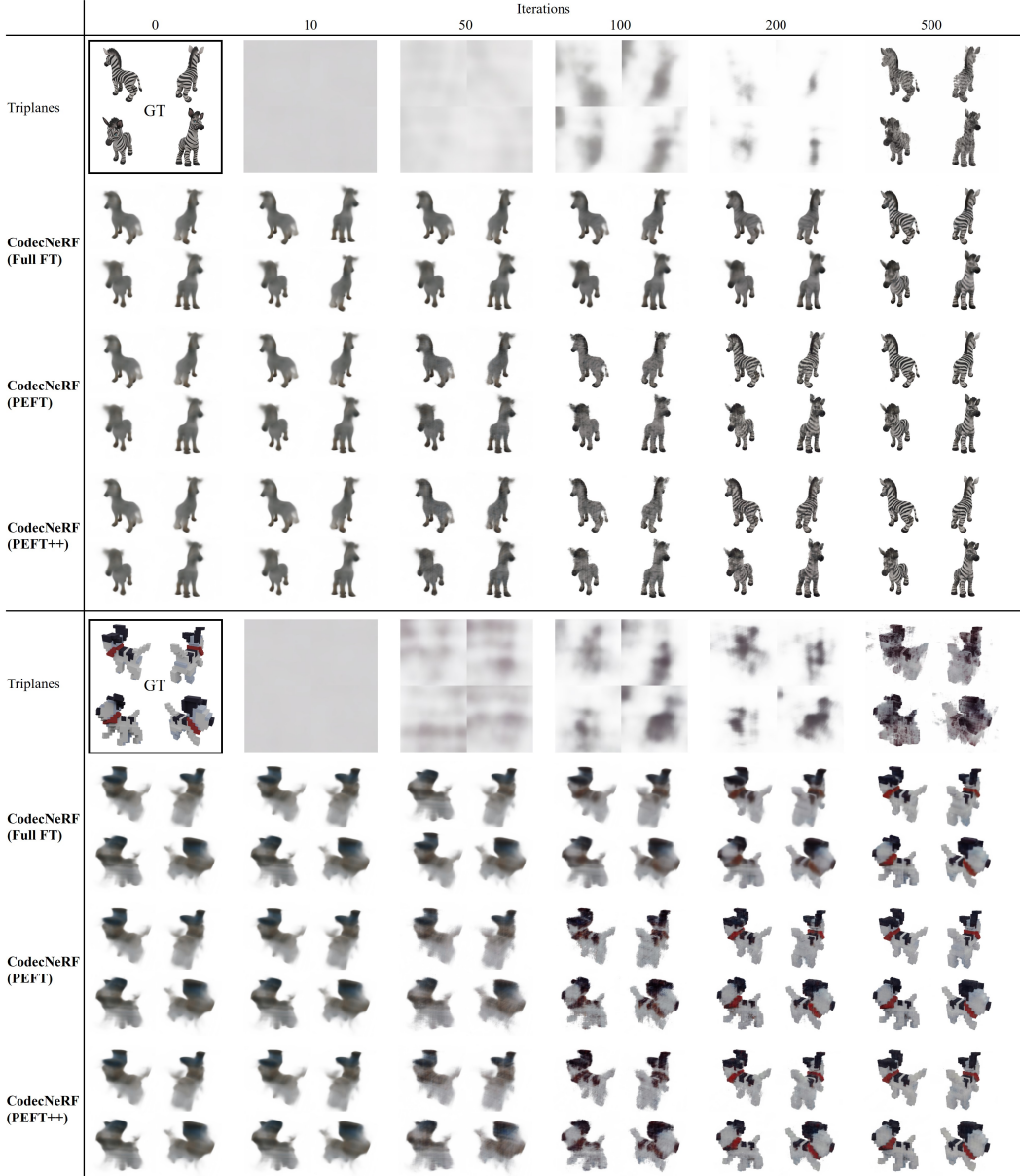


Figure 10: Novel view synthesis results on Objaverse dataset

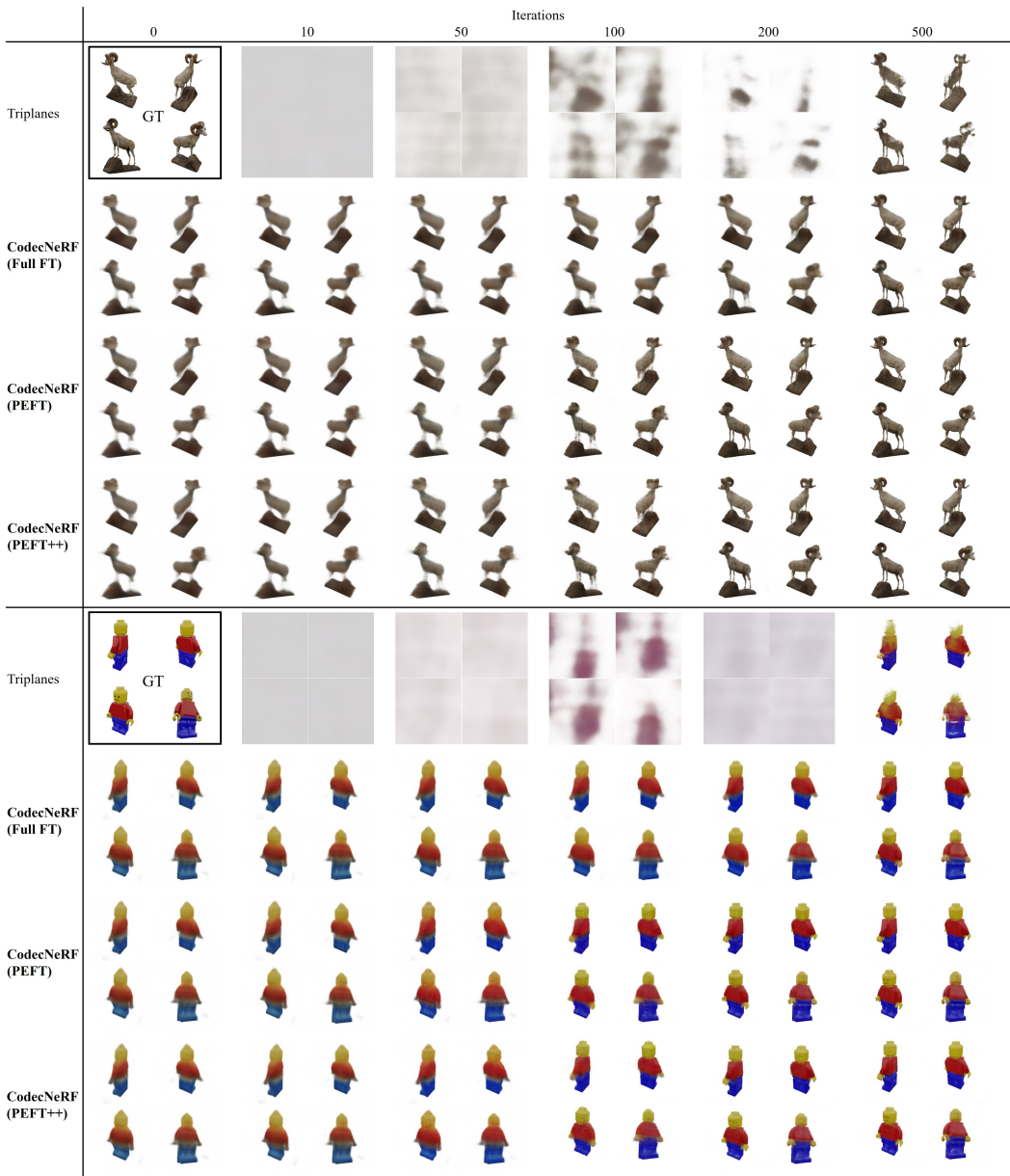


Figure 11: Novel view synthesis results on Objaverse dataset



Figure 12: Novel view synthesis results on Objaverse dataset

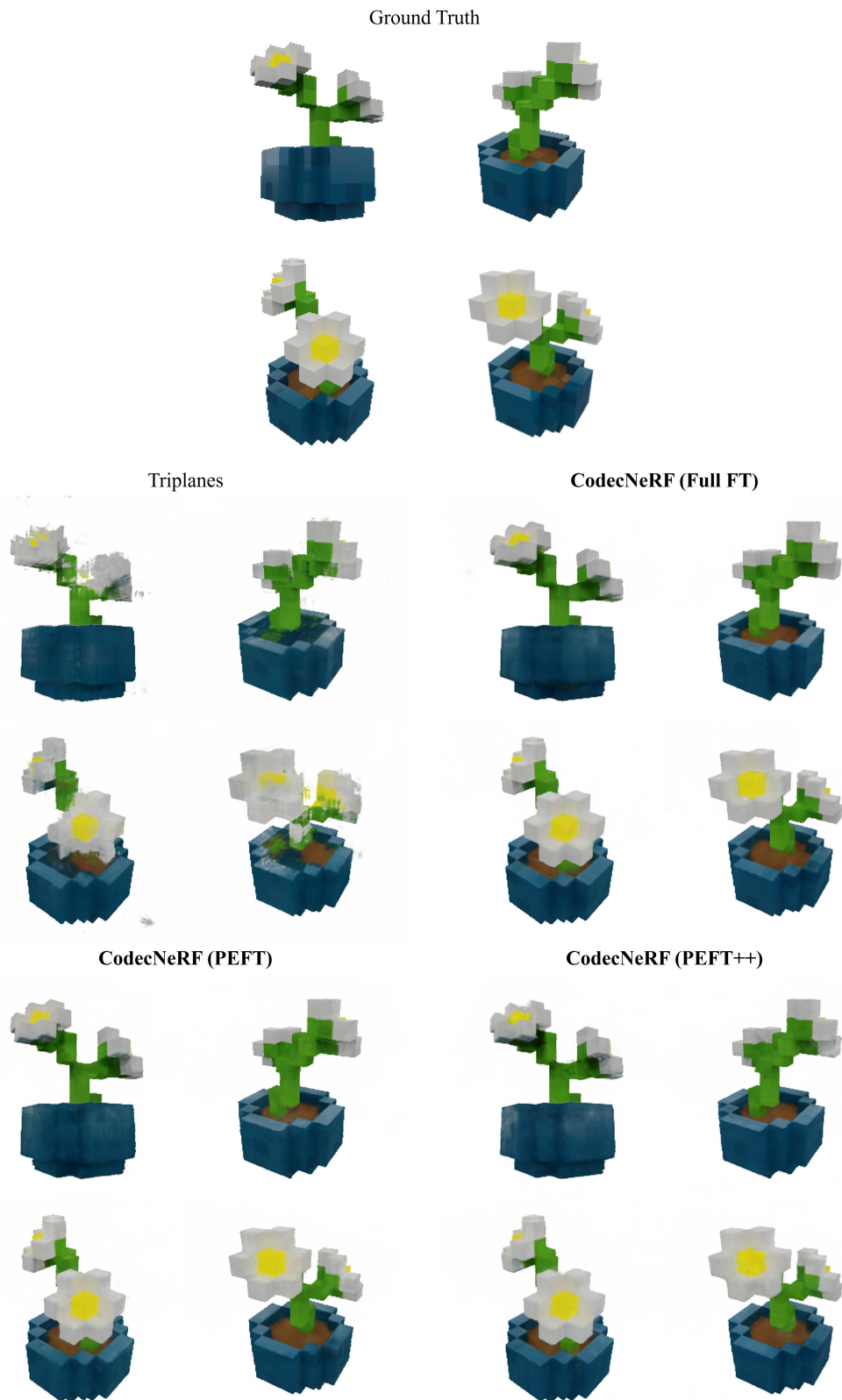


Figure 13: Novel view synthesis results on Objaverse dataset with 5000 iterations

A.3 Category-specific: ShapeNet

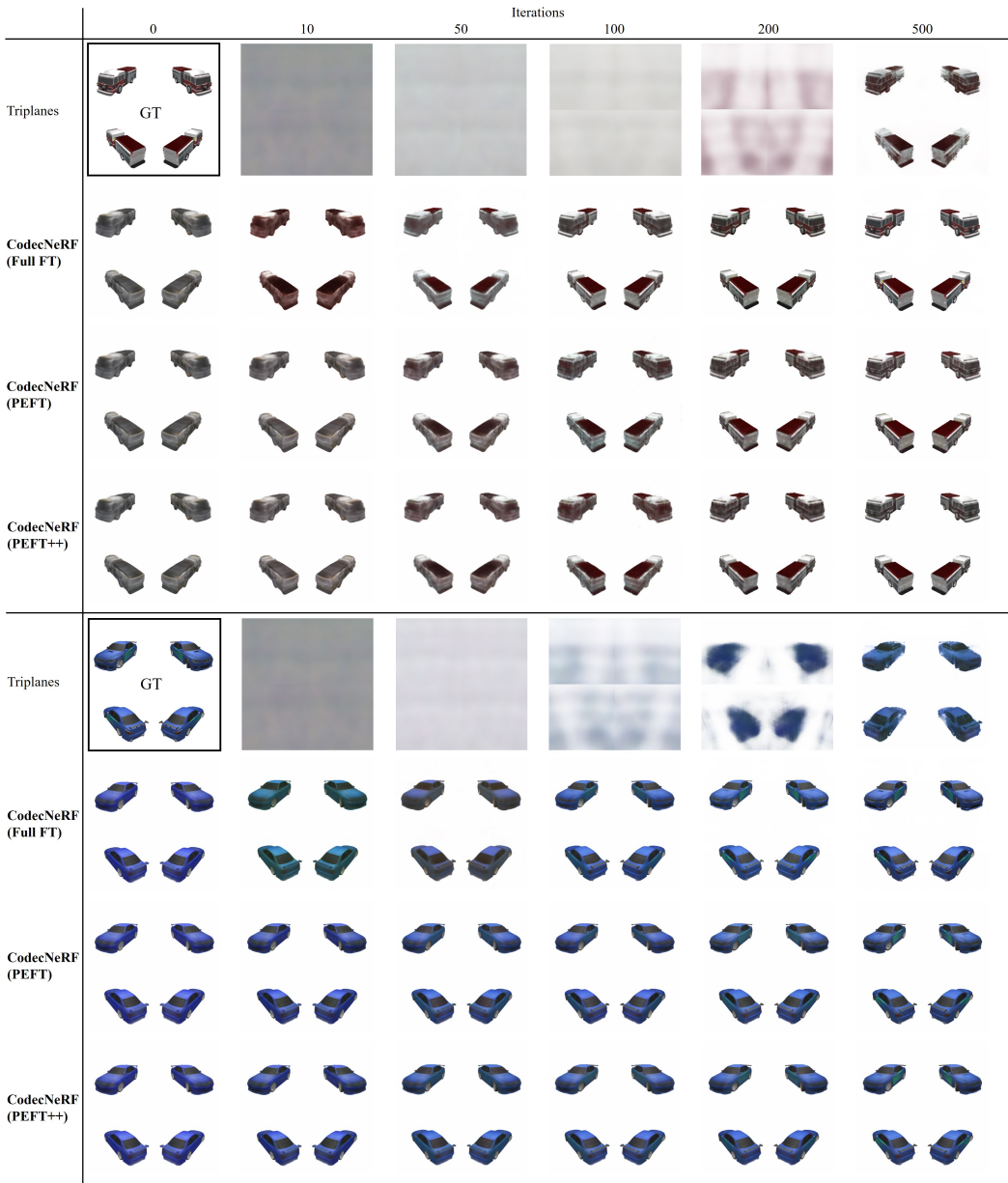


Figure 14: Novel view synthesis results on ShapeNet ‘Car’

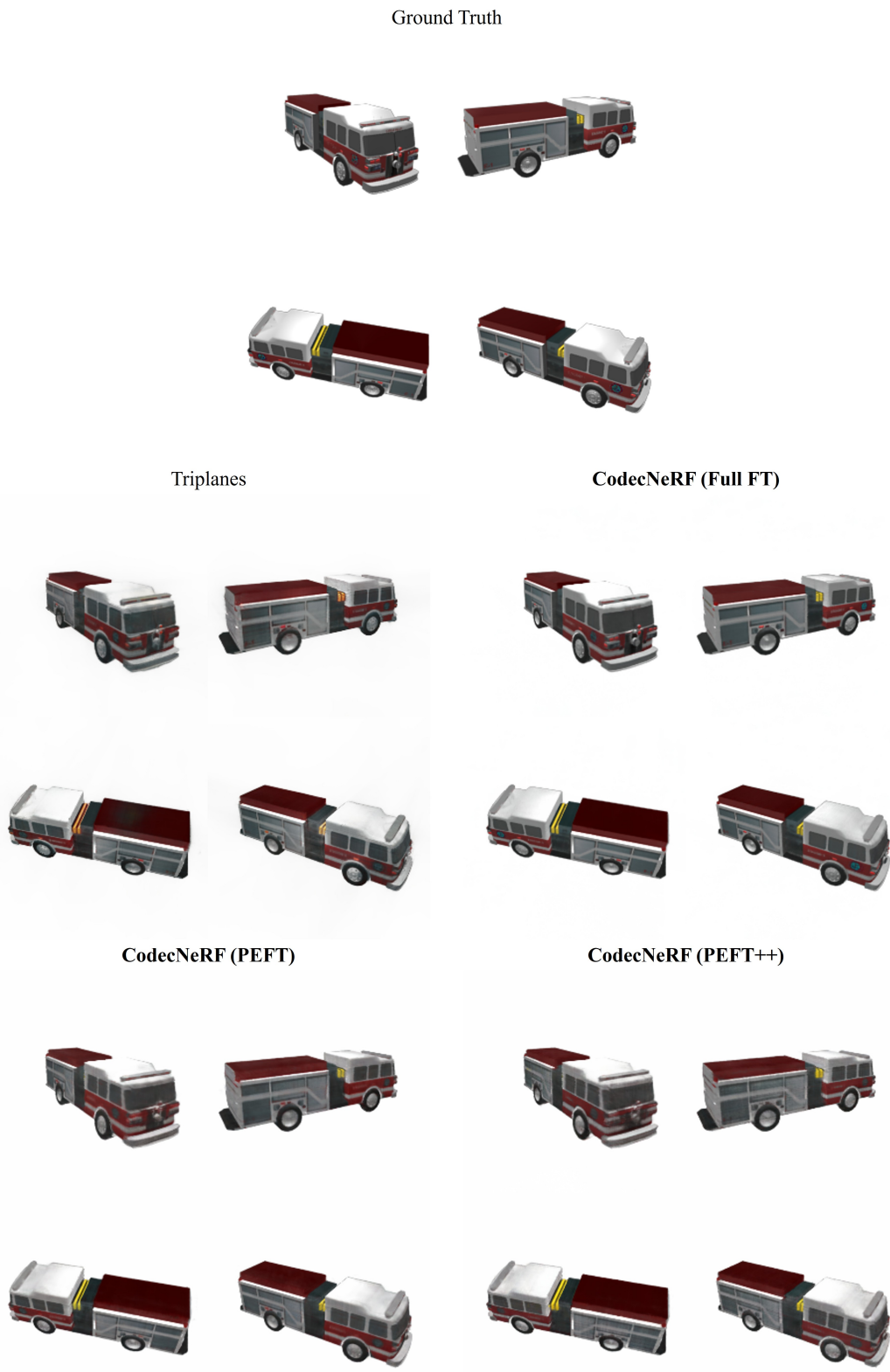


Figure 15: Novel view synthesis results on ShapeNet ‘Car’ dataset with 5000 iterations

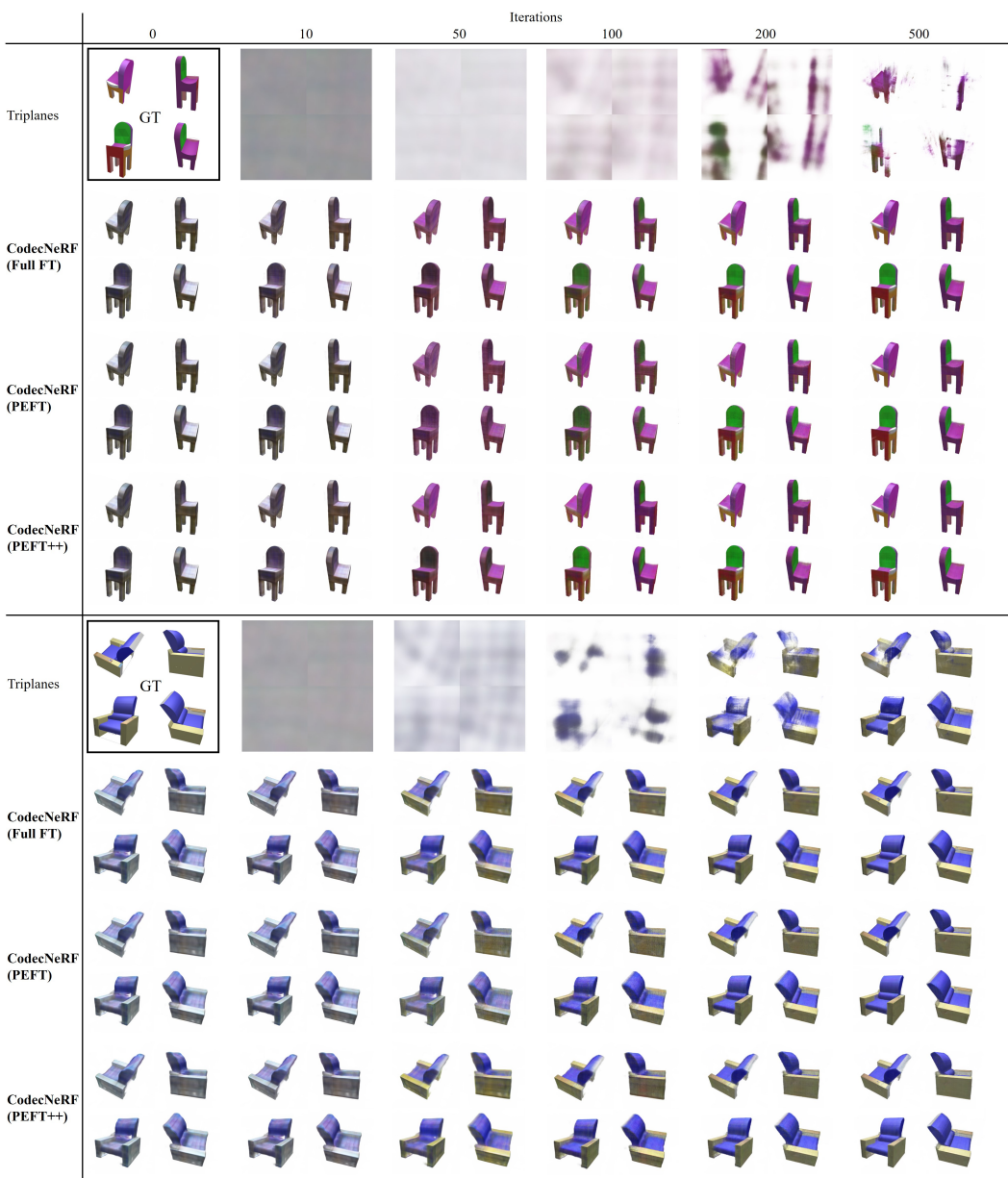


Figure 16: Novel view synthesis results on ShapeNet ‘Chair’ dataset

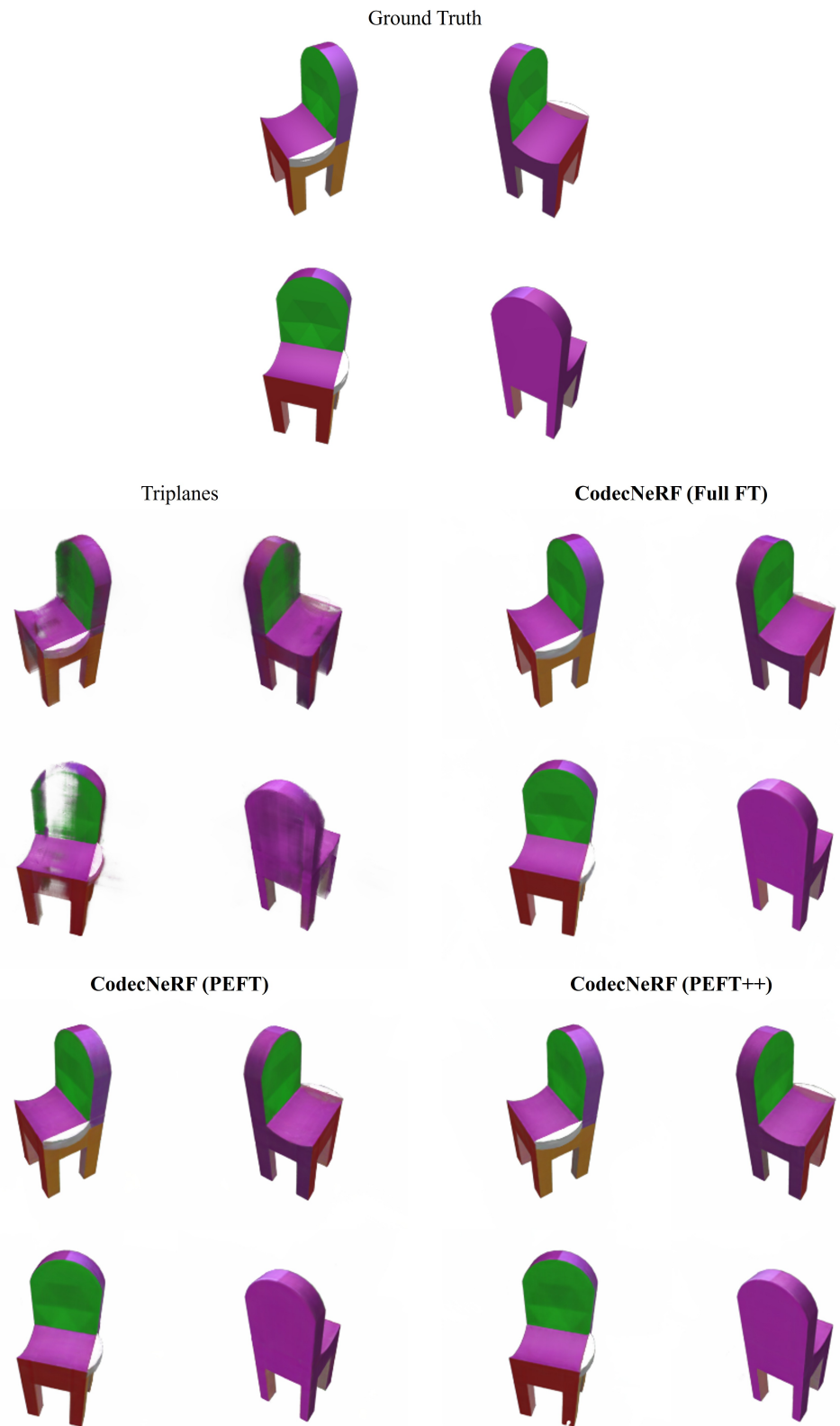


Figure 17: Novel view synthesis results on ShapeNet ‘Chair’ dataset with 5000 iterations

Table 5 and Table 6 show the component level storage used in the ShapeNet dataset, in which the rendered image resolution is 224×224 . We used the same multi-resolution triplane in main paper, but the MLP decoder is different in number of layers and hidden dimension. Please see Appendix D.3 for the details. The values in the table were measured using the same methodology as in the main paper after 10k iterations. One notable thing is the compressed triplane feature size is bigger than the Objaverse version (0.036MB). We suspected that this phenomenon came from the different capacities of the MLP decoder, and in Fig. 18, we compared the progress of feature compression with and without freezing the MLP decoder. The results showed that the gap between freezing and training MLP is bigger in the Objaverse dataset. Considering there are more MLP decoder parameters in the Objaverse model, we found that the decoder’s volume contributes to the high compression ratio of the triplane feature.

Table 5: Compression performance on ShapeNet ‘Car’ dataset.

Component	Total size in MB (codes + finetuning deltas)				
	Triplanes	Full FT	PEFT	PEFT++	W/O FT
Codebook	.	0.003	0.003	0.003	0.003
Feature	33.03	33.03	1.033	0.058	.
MLP	2.392	2.368	0.086	0.086	.
Total	35.422	35.401	1.122	0.147	0.003

Table 6: Compression performance on ShapeNet ‘Chair’ dataset.

Component	Total size in MB (codes + finetuning deltas)				
	Triplanes	Full FT	PEFT	PEFT++	W/O FT
Codebook	.	0.003	0.003	0.003	0.003
Feature	33.03	33.03	1.033	0.050	.
MLP	2.392	2.368	0.086	0.086	.
Total	35.422	35.401	1.122	0.139	0.003

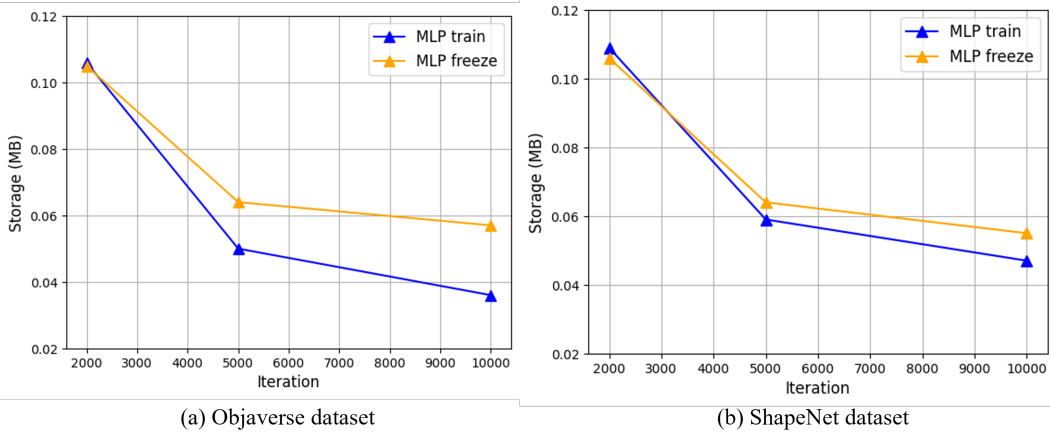


Figure 18: Triplane feature compression comparison. We used the ‘Car’ dataset for (b). We omitted the values before the 2000 iteration because the difference was almost negligible. The depicted storage sizes are only the compressed triplane feature sizes.

A.4 DTU MVS dataset

In Fig. 19, we provides additional results of novel-view synthesis using DTU dataset test scenes. As previously mentioned in main paper, we adopted PixelNeRF’s split scheme [88] to remove the overlap across the train/val/test sets and perform a more accurate cross-scene generalization benchmark. In finetuning stage, we trained our models with 1k iterations which take less than a minute. For the baseline methods, we trained 3D-GS [31] with 7k iterations and TensoRF [14] with 4k iterations. While we know the baseline models are trained for a longer duration in terms of wall-clock time, we used our configuration to evaluate the fast encoding ability. Also we only utilized the low-rank tensor decomposition method on triplanes in finetuning stage and set all decoder parameters as trainable. Due to the compact MLP decoder in DTU model (0.28MB), we still can get the highly compressed representation. For implementation details of our base DTU model and the baseline model configurations, please refer to Appendix D.4.

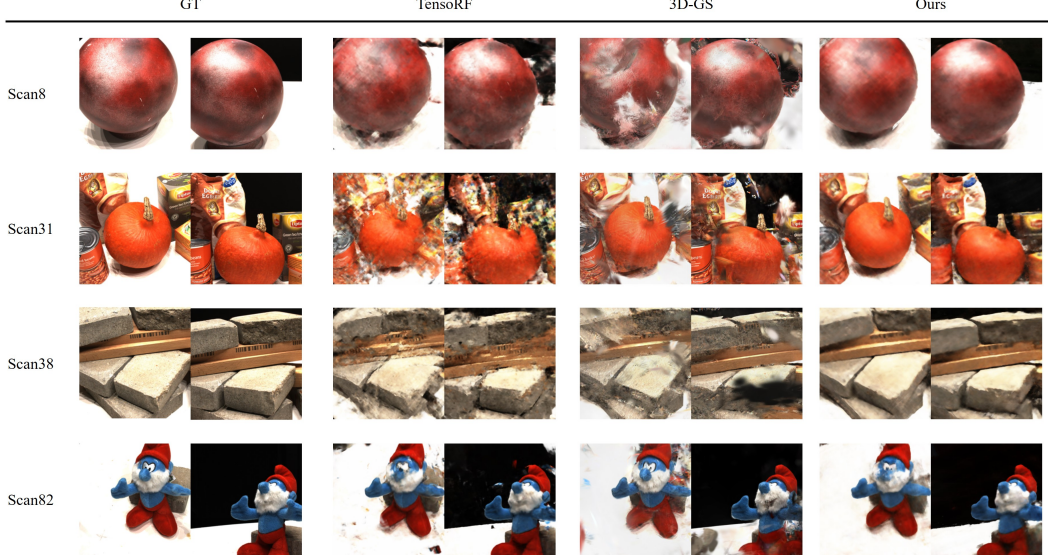


Figure 19: Novel view synthesis results on DTU MVS dataset

B Ablation studies

B.1 Tensor decomposition

In Fig. 20 and Table 7, we ablated our model on Objaverse dataset, with respect to tensor decomposition methods. The parameter-efficient finetuning method is used in experiments: all training configurations are fixed except for the tensor decomposition technique. Method **B** simply decompose the triplanes into two low-rank tensors. Taking the smallest resolution as an example, we decompose the triplane feature $\Delta\tilde{f}^1 \in \mathbb{R}^{3 \times 32 \times 64 \times 64}$ into two small tensors $h_{b1} \in \mathbb{R}^{3 \times 32 \times 64 \times 4}$ and $h_{b2} \in \mathbb{R}^{3 \times 32 \times 64 \times 4}$. We used rank number 4 for every resolution. In method **C**, we also decomposed the triplanes into 2 parts, but more parametric efficient way. Continuing with the same example as before, the feature $\Delta\tilde{f}^1 \in \mathbb{R}^{3 \times 32 \times 64 \times 64}$ is decomposed into $h_{c1} \in \mathbb{R}^{3 \times 32}$ and $h_{c2} \in \mathbb{R}^{64 \times 64}$ and only the size of h_{c2} varies as the resolution changes. We select our method considering the trade-offs between encoding speed and compression ratio.

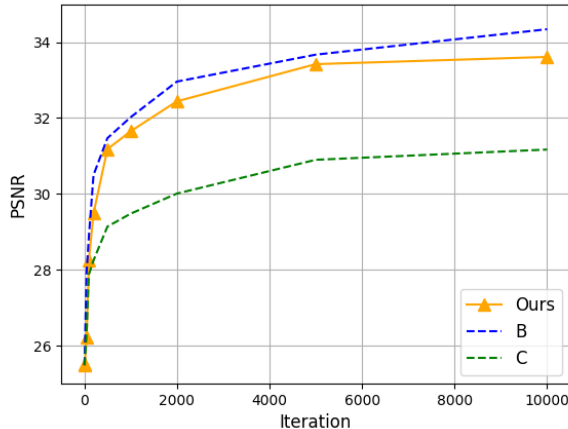


Table 7: Storage.

Method	Storage (MB)
Ours	1.033
B	1.376
C	0.345

Figure 20: Ablation study over decomposition methods.

B.2 Entropy coding on decoder

We ablated our model on Objaverse dataset, with respect to entropy coding on MLP decoder, LoRA. We used a spike-and-slab prior [67], a mixture of two Gaussians (a wide and a narrow distribution), to approximate the entropy and compress the decoder weights. As shown in Fig. 21, the code length of the LoRA weight increases along the iteration. After surpassing 1000 iterations, however, the rate of increase becomes very small, and the degradation in performance is negligible. Although it obviously requires less storage than the unapplied version, we left it out because it goes against our goal of progressive compression during the finetuning stage. We visualized the histogram of the decomposed triplane features and LoRA weights after entropy coding. Fig. 22 and Fig. 23 describe the progress of compression across the iterations.

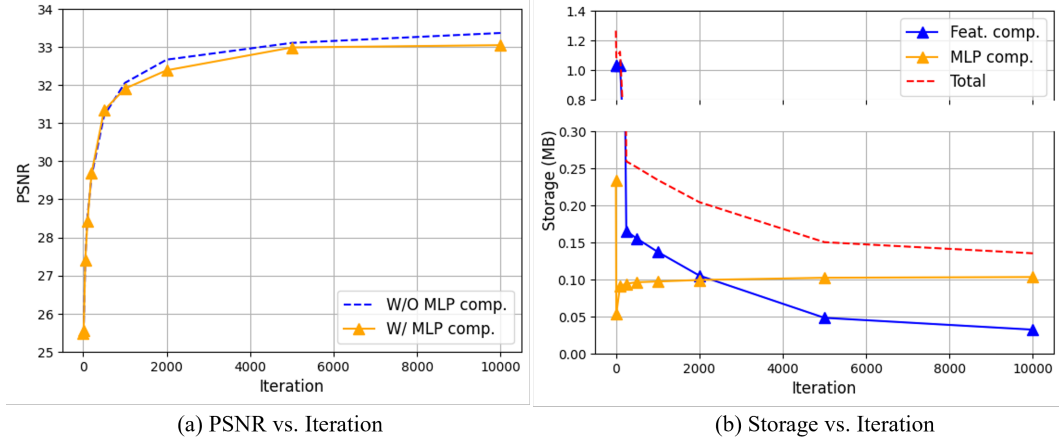


Figure 21: Ablation study over decoder compression. In the right figure, "Feat. comp." denotes triplane feature compression with our decomposition method, "MLP comp." denotes the MLP decoder compression only using LoRA weights, and the "Total" value is the sum of compressed triplane features which is decomposed and compressed LoRA weights.

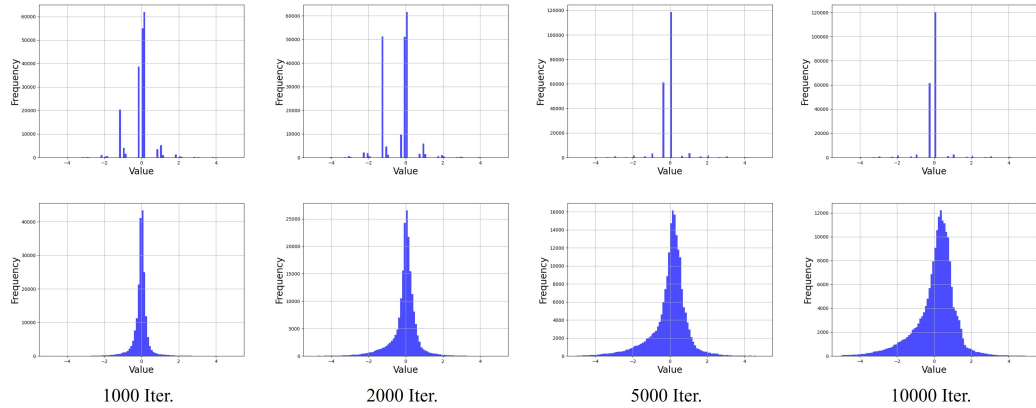


Figure 22: Feature value histogram. We used the highest resolution decomposed feature matrix $M^3 \in \mathbb{R}^{3 \times 1 \times 256 \times 256}$ for the visualization. The first row displays the histogram with entropy coding, and the next row shows the histogram without entropy coding.

B.3 Number of the rank of LoRA

In Table 8 and Fig. 24, we ablated our model on Objaverse dataset, with respect to the rank of LoRA. The experiment uses the parameter-efficient finetuning method: all training configurations are fixed except for the rank of the LoRA. The result shows that the higher rank number does not contribute to

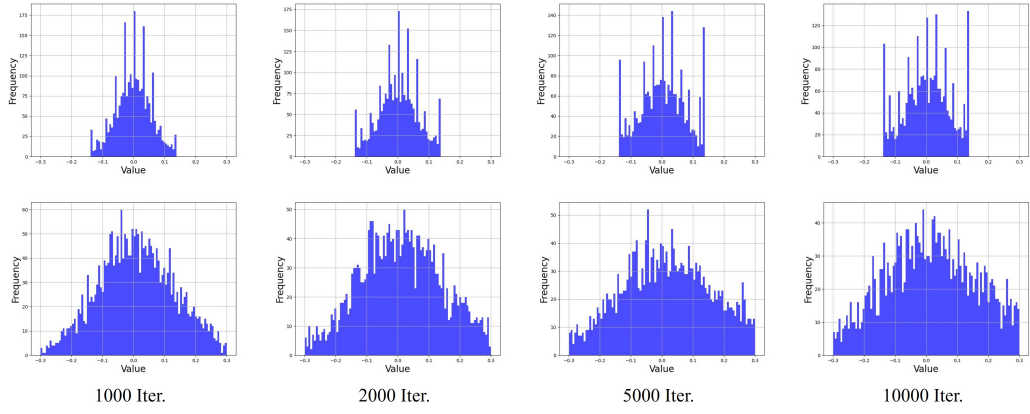


Figure 23: MLP weight histogram. We visualized the histogram with the first layer weights of LoRA. The first row depicts the results with the weight entropy model, and the next row shows the histogram without the weight entropy model.

the performance, but it makes the storage size bigger. So, we choose the rank number 4 in our whole experiment.

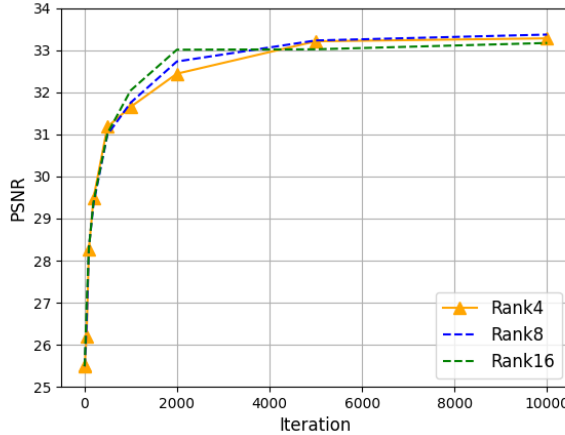


Figure 24: Ablation study over number of rank.

Table 8: Storage.

Method	Storage (MB)
Rank 4	0.233
Rank 8	0.467
Rank 16	0.934

C Additional Experiments

C.1 Generalization Performance

We additionally evaluate our method for different objectives. Table 9 shows the quantitative results compared with previous generalizable novel view synthesis methods [88, 42] which use only a single input view. While we acknowledge that our method utilizes more input views, we evaluate our method without finetuning to assess the robust generalization capabilities. Our encoder-decoder method can handle various views, enabling a more comprehensive understanding of the scene from multiple perspectives. We trained our model using the same datasets [74, 30] and evaluated without the 16 input views in each test set. For the baseline [88, 42] metrics, we re-evaluate their pretrained models.

Table 9: Generalization performance. ‘NMR’ denotes the class-agnostic ShapeNet dataset defined in [30].

Methods	Cars		Chairs		NMR	
	PSNR	SSIM	PSNR	SSIM	PSNR	SSIM
PixelNeRF	23.53	0.908	23.87	0.912	27.70	0.920
VisionNeRF	23.43	0.906	24.42	0.920	29.85	0.934
CodecNeRF	23.60	0.901	25.68	0.926	30.17	0.942

Table 10: Test time optimization comparison.

Data	Method	Iteration									
		0		50		100		200		1000	
PSNR	SSIM	PSNR	SSIM	PSNR	SSIM	PSNR	SSIM	PSNR	SSIM	PSNR	SSIM
Car	MetalINR	19.21	0.846	24.09	0.904	24.80	0.912	25.24	0.917	26.96	0.935
	CodecNeRF (FT)	23.34	0.892	24.58	0.904	25.21	0.911	26.00	0.919	27.94	0.936
	CodecNeRF (PEFT)	.	.	24.53	0.904	25.05	0.909	25.60	0.915	28.01	0.935
Chair	MetalINR	13.06	0.603	20.93	0.816	21.87	0.838	22.90	0.859	24.96	0.889
	CodecNeRF (FT)	20.24	0.803	21.74	0.831	22.63	0.850	23.86	0.874	26.69	0.915
	CodecNeRF (PEFT)	.	.	21.48	0.827	21.97	0.840	22.84	0.855	25.83	0.902

C.2 Comparison to Meta-initialization

Also, we access our initialization and test time optimization with MetalINR [79]. For a fair comparison, we set the same training scheme from scratch only except for the meta learning method. Specifically, 24 images are used to train the based model, also the same number of images are used for test time optimization, and remaining 26 views are evaluated for the metrics. Table 10 shows the quantitative results, and our method shows faster convergence from initialization even in parameter efficient setting.

C.3 Details

We changed the multi-resolution triplane feature in Generalization and Meta-initialization experiments. In the results depicted in Table 9 and Table 10, the ‘Cars’ and ‘Chairs’ datasets have a resolution of 128×128 , and the ‘NMR’ dataset has a resolution of 64×64 . We used two-resolution triplanes for the experiments when training low-resolution datasets, as opposed to default three-resolution triplanes. We used triplanes resolutions of $\{64, 128\}$ for the image resolution of 128×128 , and $\{32, 64\}$ for the image resolution of 64×64 .

D Reproducibility

D.1 3D-aware 2D convolution

As briefly discussed in the main paper, we use a hierarchical 3D-aware 2D convolutional block to process the triplane features while respecting their 3D relationship. To compute for new XY plane while attending to all elements in YZ and XZ planes, we perform axis-wise average pooling to YZ (along Z axis) and XZ (along Z axis) planes, resulting in two feature vectors. Then, aggregated vectors are expanded to the original 2D dimension by duplicating along the axis, concatenated with XY plane channel-wise, and we perform a usual 2D convolution. The same procedure is applied to YZ and XZ planes. The overall architecture is depicted in Fig. 25, and we generate multi-resolution triplanes in a hierarchical manner.

D.2 ResNet style 2D convolution

We employ a ResNet style 2D convolution block to each multi-resolution triplanes, generated from Appendix D.1. This architecture is illustrated in Fig. 26, and we can interpret this procedure as refining the triplane features before feeding into the MLP decoder.

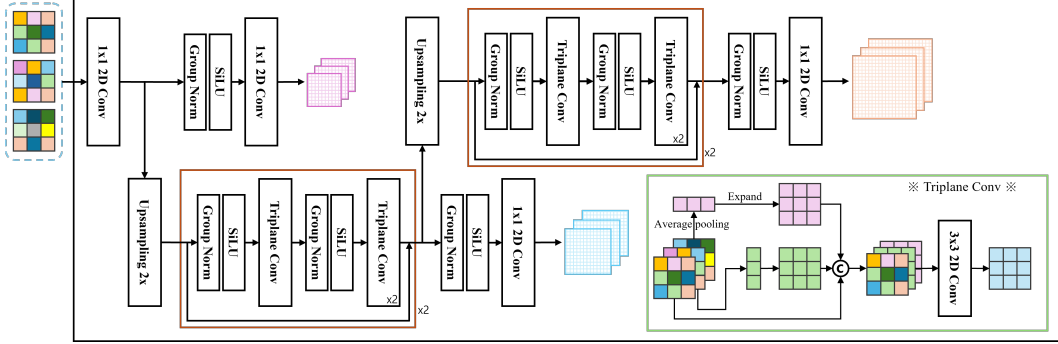


Figure 25: 3d aware 2D convolution block.

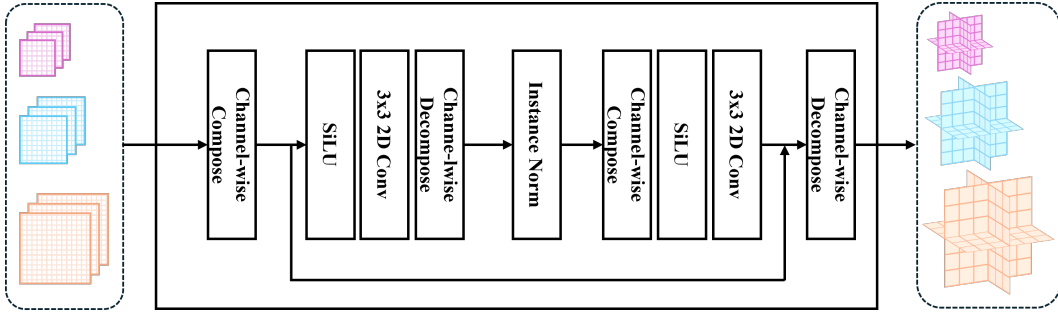


Figure 26: ResNet style 2D convolution block.

D.3 Triplanes architecture

As described in Section 4.3 of the main paper, we set our baseline model ‘Triplanes’ which is modified from K-planes [21]. The following material will cover each component of our ‘Triplanes’ in detail.

D.3.1 Resolution size

For the multi-resolution triplanes representation, we use three rectangular spatial resolutions, $\{64, 128, 256\}$ as default. We employed the same size in both the Objaverse and ShapeNet datasets.

D.3.2 Decoder size

We also matched the MLP decoder size, 1) Objaverse: 512 hidden dimensions, 8 fully-connected layers, and 2) ShapeNet: 256 hidden dimensions, 6 fully-connected layers. As opposed to conventional triplane models [12, 21, 84] using lightweight decoders (usually 4 fully-connected layers), our model has a larger MLP network. We found that increasing the MLP size is important to performance both in base model training and fine-tuning.

D.3.3 Decoding method

We used vanilla NeRF [54] decoding method in all experiments which uses coarse MLP and fine MLP, both with identical architectures. We first sample 64 points using stratified sampling and then generate important 64 points that are biased towards the relevant surface of the volume, given the output of coarse MLP. We have trained our model using proposal sampling strategy [6, 21], but we found that the decoder weights became excessively small, leading to model destabilization even with minor variations in the finetuning stage.

D.4 More Implementation Details

We used three spatial resolutions $\{V_1, V_2, V_3\} = \{64, 128, 256\}$ and channel size $C = 32$ for our multi-resolution triplanes for Objaverse and ShapeNet dataset. For category-specific training, we set the codebook size $K = 1024$ and the codebook dimension $C' = 16$. In the category-agnostic version, the codebook size is increased to 4096 while the dimension remains the same for the compact representation. Also, considering the capacity of our model, we double the size of the hidden layer dimension from 256 to 512 in the MLP decoder when training the Objaverse dataset.

For DTU dataset, we used two resolutions triplanes $\{V_1, V_2\} = \{64, 128\}$ with 32 channel dimensions and 4096 codebook size with 32 codebook dimensions. Also we replaced the feature extractor from [43] to widely used pretrained ViT model [11], applied attention blocks in bottleneck layers and decreased the decoder layer’s hidden dimensions to 64. The baseline model configurations used for DTU dataset are as follows: 1) 3D-GS [31]: We generated 50k random initial point cloud and trained with default settings. 2) TensoRF [14]: We trained the model with default settings. All models are trained on a single H100 GPU.

For in-depth compression evaluations, we used two voxel-form baseline models, MaskDWT [64] and VQRF [40]. We trained with default settings and all experiments are trained with 10k iterations (VQRF is trained with additional 10k iterations for the post vector quantization model.). However, vanilla MaskDWT showed results 28.68 PSNR with 11.21MB. With respect to the intent of the experiment about compact 3D representation, we downscaled the voxel resolution to 128 dimension and used the results (26.74 PSNR with 2.93MB). Also evaluation in terms of training speed, we regulated the coarse and fine iterations in DVGO [76] to match the default ratio. Specifically, when we evaluate the test view performance in early stage, we decreased the coarse and fine numbers in a original proportion. Except for the change we keep the original configurations. All models are trained on a single H100 GPU.